THERMAL CONTACT RESISTANCE AT THE SNOW-ICE INTERFACE:

DEPENDENCE ON GRAIN SIZE

by

Michael Alan Dvorsak

A thesis submitted in partial fulfillment
of the requirements for the degree

of

Master of Science

in

Mechanical Engineering

MONTANA STATE UNIVERSITY
Bozeman, Montana

May 2022

©COPYRIGHT

by

Michael Alan Dvorsak

2022

All Rights Reserved

TABLE OF CONTENTS

TABLE OF CONTENTS – CONTINUED

LIST OF TABLES

Table Page

LIST OF FIGURES

LIST OF FIGURES – CONTINUED

LIST OF FIGURES – CONTINUED

NOMENCLATURE

ρ	Density ($kg\ m^{-3}$)
c_p	Specific heat capacity at constant pressure ($JK^{-1}kg^{-1}$)
T	Temperature (°C)
t	time (s)
$q_{conduction}$	Heat flux due to conduction (Wm^{-2})
$q_{latentheat}$	Heat flux due to latent heating (Wm^{-2})
k	Thermal conductivity ($Wm^{-1}K$)
J_z	Water vapor flux ($kg\ m^{-2}s^{-1}$)
L	Latent heat of sublimation ($J\ kg^{-1}$)
D_{H_20}	Diffusivity of water vapor in air ($m^2\ s^{-1}$)
M_{H_20}	Mass of a water molecule (kg)
ΔC_z	Gradient of vapor pressure ($Pa\ m^{-1}$)
e_b	Equilibrium vapor pressure (bottom) (Pa)
e_t	Equilibrium vapor pressure (top) (Pa)
z	Height (m)
T_m	Mean temperature (K)
k_b	Boltzmann constant ($J\ K^{-1}$)
ΔT	Temperature change (°C)
R_{tot}	Total thermal resistance ($m^2\ K\ W^{-1}$)
Q_{tot}	Total heat flux (Wm^{-2})
$q_{contact}$	Heat flux through contact points (Wm^{-2})
q_{gap}	Heat flux through gaps (Wm^{-2})
$Q1$	Heat flux at region 1 (Wm^{-2})
$Q2$	Heat flux at region 2 (Wm^{-2})
$Q3$	Heat flux at region 3 (Wm^{-2})
$Q4$	Heat flux at region 4 (Wm^{-2})
R_C	Thermal resistance due to conduction ($m^2\ K\ W^{-1}$)
R_{TCR}	Thermal contact resistance ($m^2\ K\ W^{-1}$)

ABSTRACT

Seasonal snow covers consist of many stratigraphic layers of varying density and, therefore, thermal conductivity. Weak layers can develop at the interface between these snow layers, reducing stability and increasing avalanche danger. While it is known that a bulk temperature gradient of $-10°C\ m^{-1}$ across a snowpack enhances weak layer development via kinetic snow metamorphism, recent studies have identified an enhancement of this temperature gradient across snow interfaces. Previous work has determined that at a snow-ice interface, such as might exist around ice crusts in the snowpack, the driving factor for a temperature gradient enhancement could be a thermal contact resistance. This creates an interfacial phenomenon that induces a large temperature drop at the interface between two connected materials. The primary mechanism is a reduction of contact area for conduction to occur due to the porous nature of snow. Here, we further investigate the thermodynamics of a snow-ice interface by varying the grain size, which directly correlates to the total contact area. Within a controlled laboratory environment, a 4 mm ice lens was artificially made and placed between rounded grains that varied in size (1, 2, and 3 mm) between experiments. Temperature gradients of -10, -50, and $-100°C\ m^{-1}$ were then applied across the sample. The temperature gradient was measured in-situ within 1 mm of the ice lens using micro-thermocouple measurements. The local temperature gradient at the snow-ice interface was found to be up to four times the imposed temperature gradient with 2-3 mm snow grains and near the bulk temperature gradient with the 1 mm grains. Following a thermal analysis, it was concluded that the enhancement in the temperature gradient was also due to a thermal contact resistance at the snow-ice interface. Utilizing time-lapse x-ray computed microtomography, a microstructural characterization of the snow-ice interface was also performed, where it was observed that new ice crystal growth, kinetic snow metamorphism, and sublimation were all occurring simultaneously near the ice lens. These results indicate that the observed grain size near an ice lens or crust in a natural snowpack may be a pertinent parameter for better understanding kinetic snow metamorphism regimes that may exist at these interfaces.

CHAPTER ONE

INTRODUCTION

Snowpack stability has significant implications on transportation and human fatalities due to the large amounts of avalanches that occur each year [31, 40]. As humans move into more cryospheric environments, avalanche hazards become of greater concern. Avalanches occur due to a weak layer in the snowpack, if the snow above becomes cohesive and fractures, it will slide on the weak layer. This type of avalanche is considered a slab avalanche and can release on a weak layer consisting of poorly bonded faceted snow crystals [26]. Faceted snow forms due to a process known as kinetic snow metamorphism and is caused by a temperature gradient (TG) inducing water vapor flow in the snowpack [32]. Ice crusts, also known as ice lenses, can develop a weak layer that slab avalanches occur on and can persist throughout a season once formed [36, 37]. An ice crust typically forms during a warming or rain event and creates faceted crystals above and below, making it a favorable area for a snow slab to fracture and avalanche [18].

Previous studies have investigated the processes by which heat and mass move through a homogeneous snowpack and its effect on snow metamorphism [2, 16, 27, 34, 42] or the mechanical stability of a layered snowpack [6, 14]. However, few have combined these two aspects, observing how 1) heat and mass transfer through a layered snowpack and 2) affects stability. Theoretical models have speculated on the processes that occur, but lack physical evidence [3, 13]. Greene (2007) performed TG laboratory studies using ice crusts created in the lab and collected from the field, attempting to understand the effects on snow metamorphism [19]. These experiments provided observations that were indicative of a enhanced TG at the snow-ice interface. Although there was an attempt to measure the TG at the the interface, it was unsuccessful due to the lack of spatial resolution of the thermocouples (1 cm). This investigation into ice crusts was continued about a decade later by Hammonds et al. (2015), utilizing more advanced techniques such as time-lapse X-ray computed micro-tomography (micro-CT), scanning electron microscopy, and in-situ micro-thermocouple measurements within 1 mm of an ice lens [20, 23]. This study observed TG's up to 40 times the imposed gradient at the snow-ice interface, concluding that a thermal contact resistance was responsible. The thermal contact resistance is a phenomenon that occurs at an interface between two solids and is influenced by the contact area of an imperfect bond [5, 39]. It describes how heat converges at the area of contact and resists heat flow between the two materials, resulting in an increase in the TG at the interface. In theory, the local TG at the snow-ice interface would be directly influenced by the snow grain size, given that as the grain size increases, the total contact area decreases. Due to the effect of a thermal contact resistance, the TG would be expected to increase at the snow-ice interface.

The goal of this study was to investigate the effect snow grain size has on the local TG above and below an ice lens. Hammonds et al. (2015) measured the temperature profile of one snow grain size (2.5-3 mm) and one ice lens thickness (4 mm). If the enhanced TG at the snow-ice interface were due to a thermal contact resistance, as theorized by Hammonds & Baker (2016), then the TG measurements at the snow-ice interface should vary drastically with the snow grain size. Which would be due to the reduction in total contact area between the snow and ice as the grain size increases. To understand this process, similar methods were utilized from Hammonds et al. (2015 & 2016), which include in-situ temperature measurements within 1 mm above and below the ice lens, time-lapse micro-CT, and a thermal analysis. Samples were housed in a 50 mm tall plastic tube with a 4 mm ice lens in the center and varying snow grain sizes (1, 2, and 3 mm) above and below. Thermocouple measurements were achieved by subjecting the specimen to multiple temperature gradients (-10, -50, and -100°C m^{-1}) and allowing thermal steady-state conditions to occur. This process was repeated multiple times for each snow grain size. In a parallel set of experiments, microstructural characterization utilized micro-CT imagery every 12H over a 48H test period while the sample was placed under a $-100°\text{C m}^{-1}$ TG.

CHAPTER TWO

BACKGROUND

2.1 Heat and Vapor Transport in Snow

Heat and water vapor constantly move between snow grains and throughout a snowpack due to mass, heat, and stress gradients. In seasonal snowpacks, the base is typically warmer (0°C) than the snow surface, which fluctuates with atmospheric conditions [4, 29]. The temperature difference creates a TG which causes heat and water vapor to generally flow from the bottom to the top of the snowpack. Because of the large magnitude of transport from the bottom to the top, the system can be reduced to one dimension, correlating to the z-direction (vertical) in a Cartesian coordinate system. Based on the assumptions above, a general equation can be derived for the heat transfer in a snowpack, shown in Equation 2.1 [19]. Where ρ ($kg\ m^{-3}$) is density, c_p ($JK^{-1}kg^{-1}$) is the heat capacity at a constant pressure, T (K) is temperature and t (s) is the time over which the temperature changes. The overall heat flux (Wm^{-2}) is reduced to the heat transported via conduction $q_{conduction}$ and from latent heat $q_{latentheat}$.

$$\rho c_p \frac{\partial T}{\partial t} = -\frac{\partial}{\partial z} \cdot (q_{conduction} + q_{latentheat}) \tag{2.1}$$

It should be noted that the convective heat flux is not included in Eq. 2.1, even though recent findings suggest that it may be of relevance to the microstructural evolution [17]. However, substantial evidence does not currently exist to include a convection term and this thesis will follow previous studies by neglecting convection as a mode of heat transfer [19, 20, 23]. Using Fouriers Law [5], $q_{conduction}$ is represented in Equation 2.2, where k ($Wm^{-1}K$) is the thermal conductivity specific to a material. Due to the porous nature of snow, the thermal conductivity is not constant and an effective thermal conductivity must be used. The effective thermal conductivity can be calculated using a numerical solution as a function of snow density (Equation 2.3) [8]. The other form of heat flux is the heat released from the process of sublimation and deposition, formally known as latent heat. Using Fick's law of diffusion, the heat transfer can be represented by Equation 2.4 [38], where J_z (kg $m^{-2}s^{-1}$) is the water vapor flux in the z-direction and L ($J\ kg^{-1}$) is the Latent Heat of Sublimation.

$$q_{conduction} = -k_{eff}\frac{\partial T}{\partial z} \tag{2.2}$$

$$k_{eff} = 2.5 \times 10^{-6}\rho^2 - 1.23 \times 10^{-4}\rho + 0.024 \tag{2.3}$$

$$q_{latentheat} = J_z L \tag{2.4}$$

Calculating J_z utilizes the constitutive mass transfer Equation 2.5 [38], where D_{H_20} ($m^2\ s^{-1}$) is the water vapor diffusivity, M_{H_20} (kg) is the mass of a water molecule, and ΔC_z ($Pa\ m^{-1}$) is the water vapor pressure. ΔC_z was calculated by using the difference in the equilibrium pressures at the bottom e_b (Pa) and the top e_t [33], z (m) the sample height, T_m (K) mean temperature and Boltzmann's Constant k_b ($J\ K^{-1}$). The equation for the equilibrium vapor pressure (e_b or e_t) is located in Appendix B, Equation B.1.

$$J_z = D_{H_20}\Delta C_z M_{H_20} \tag{2.5}$$

$$\Delta C_z = \frac{|e_b - e_t|}{z k_b T_m} \tag{2.6}$$

Understanding the fundamental equations above is pertinent to describing the processes snow undergoes at the micro-scale. They will ultimately be the foundation for interpreting the thermophysical properties at the snow-ice interface.

2.2 Dry Snow Metamorphism

The properties of dry snow are constantly changing due to the close proximity to its melting temperature and a generally high specific surface area (SSA) [11]. When a snowpack is isothermal, there are differences in the local curvature and stress, that create localized water vapor and heat transport. This creates minuscule temperature and water vapor differences, inducing thermodynamic metamorphism in the local snow grains such as slow grain coarsening and necking. The small magnitude of growth does not compare to the TG caused by cold temperatures at the surface. These large TG's are generally one-dimensional from the bottom to the top because of the insulating properties of snow [10]. A TG also induces a vapor pressure gradient, which occurs because the bottom of each snow grain is warmer than the top (Figure 2.1). Based on Equation B.1, the equilibrium vapor pressure of ice increases with temperature, which brings about sublimation on top of the snow grain (warmer side) and deposition on the bottom of the grain above. This method of water vapor movement is referred to as hand-to-hand transport [43]. Laboratory studies and theoretical models support this theory of water vapor flow [11]. However, recent findings suggest the methods should be a "growth by replacement" instead [34]. They also showed that 60% of the total ice mass sublimated and redeposited each day, suggesting that larger grains were dominating while the smaller grains experience rapid sublimation. This results in water vapor having the ability to diffuse between grains and flow upwards with the TG. When the water vapor flux lies below a critical supersaturation, which correlates to a TG of around $-10°\text{C m}^{-1}$, the snow grains undergo equi-temperature metamorphism [29]. This is typically referenced as rounding snow grains because the grains are moving toward a more energy favorable state with low curvature and SSA. Rounded grains are shown in Figure 2.2a, which form strong bonds between each other and over time create a mechanically stable snowpack [12].

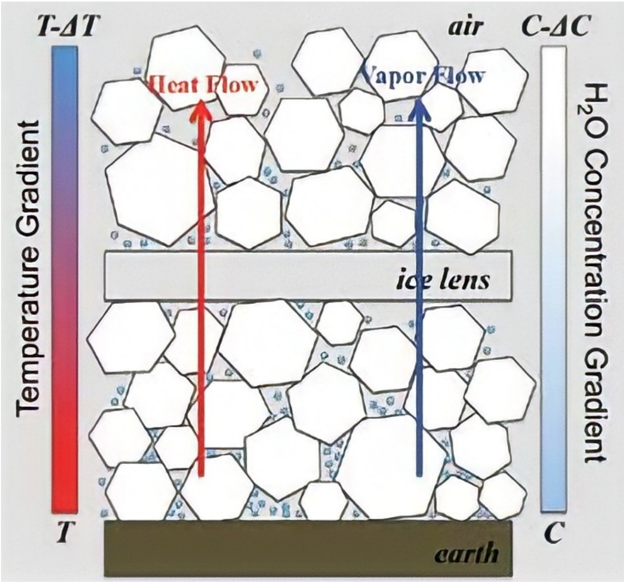

Figure 2.1: An illustration of heat and vapor flowing through a snowpack with an ice lens in the middle [22].

When the supersaturation is large enough to induce rapid growth rates, water vapor deposits onto existing snow grains as sharp angular deposits [11]. This type of growth is termed kinetic snow metamorphism and occurs when a TG above $-10°\text{C m}^{-1}$ is present. During the growth process, snow grains become sharp and angular over time, illustrated in Figure 2.2b, this subsequently increasing the SSA. Other factors that induce faster kinetic snow metamorphism are high porosity's and warmer temperatures (i.e. near the ground) [11]. Kinetic snow metamorphism is primarily dependant on the TG and can occur rapidly if large TG's are present. Predicting the rate at which this process will occur is relatively rudimentary in a homogeneous snowpack. However, once variation is introduced, such as snow stratigraphy, the system becomes much more difficult to model.

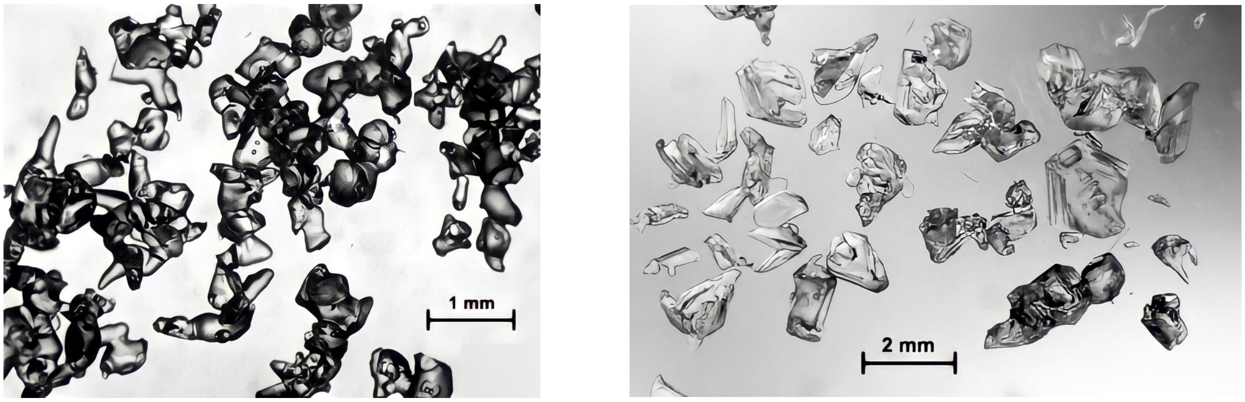

(a) Large Rounded Snow Grains (b) Faceted Snow Grains

Figure 2.2: Images from optical microscopy of two different snow grain types [15].

2.3 Thermal Contact Resistance

Heat and electricity transport can be characterized similarly, just as there is an electrical resistance that impedes the flow of current, there is also a thermal resistance. The conventional forms of thermal transport such as conduction, convection, and radiation all have equations that describe the resistance to the flow of heat due to the material and environmental conditions. Equation 2.7 shows the mechanism of finding the total heat transport across a system, where Q ($W\ m^{-2}$) is the total heat flux, ΔT (K) is the difference in temperature from the bottom to top and R_{tot} ($m^2\ K\ W^{-1}$) is the total resistance [5].

$$Q_{tot} = \frac{\Delta T}{R_{tot}} \tag{2.7}$$

However, some resistances occur which are unconventional and cannot be described by the material's properties. For instance, when two materials are joined together the connection is not perfect and will have pockets of fluid, such as air. The thermal conductivity of air ($0.024\ W\ m^{-1}K^{-1}$) is typically orders of magnitude lower than the solid material that heat is flowing through. This constricts the heat to any contact area between the two materials, creating a large temperature drop, illustrated in Figure 2.3 [5].

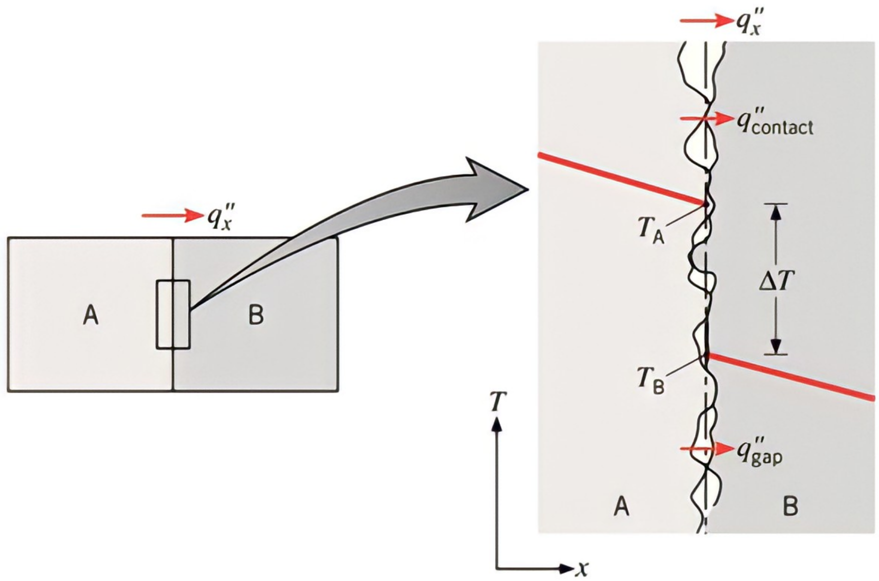

Figure 2.3: An illustration of the heat flow across two materials A and B, on the right shows the interface zoomed in and the temperature drop that occurs due to a thermal contact resistance [5].

$$R_{TCR} = \frac{\Delta T}{q_{contact} + q_{gap}} \tag{2.8}$$

A thermal contact resistance is considered an interfacial phenomenon, which can only be found experimentally using Equation (2.8) [5, 39]. Figure 2.3 visually describes the variables in Equation 2.8, where ΔT is the change in temperature at the interface, $q_{contact}$ and q_{gap} are the heat flux across the contact area and void space, respectively. Although q_{gap} is included in the calculation, when air resides in the gap, it results in an insignificant heat flux and is neglected. Thermal contact resistance is addressed by increasing the area of contact; a common technique is using a filler such as thermal epoxy.

The major implications of a thermal contact resistance are that it increases the local TG significantly and impedes heat flow at the interface. For many experimental purposes, the interface is not spatially finite and the height needs to be solved, by considering other modes of thermal transport. If such a large drop in temperature were present in a snowpack due to a interfacial resistance, one would also expect to see an increased rate of kinetic snow metamorphism at the localized area of the interface. An example of this would be a snow-ice interface, where the convergence of heat flow is illustrated in Figure 2.4 [23].

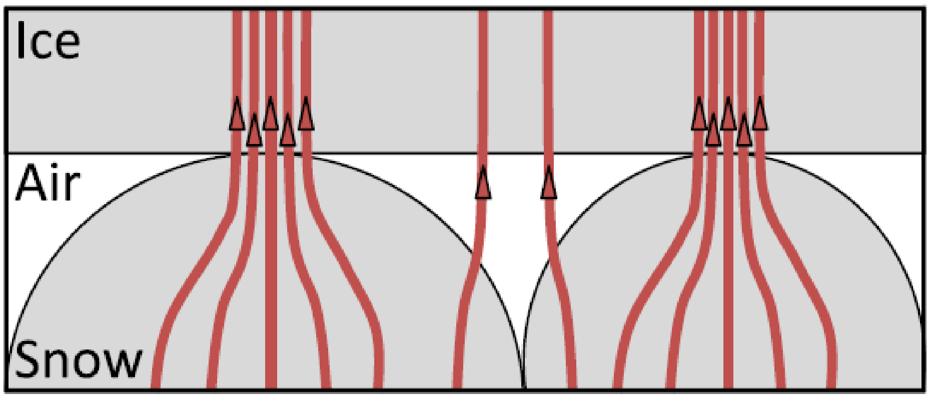

Figure 2.4: Illustration of the heat flow paths converging while moving from snow grains to solid ice [23].

2.4 Previous Work Investigating The Snow-Ice Interface

Weak layer development at an ice crust or ice lens has been observed visually in the field for many years and has been the cause of many avalanches [15, 26]. Theory's have been established as to why the weak layer develops [10, 13], most of which remain purely theoretical. The first physical study to investigate this was done by Greene (2007), where a series of experiments were performed, which consisted of laboratory measurements utilizing natural snow and artificial ice crusts [19]. Greene put his samples under a large temperature gradient ($> 60°\text{C m}^{-1}$) with thermocouples embedded, while also utilizing heat flux sensors to measure the heat flux at the top and bottom. After each experiment, the sample was cast using dimethly phthalate, then serial cross-sectioned to achieve 3D reconstructions and microstructural parameterization. Greene found that 1) the upper surface of the ice lens eroded, leaving behind a round and smooth surface, 2) ice crystals formed on the bottom of the ice lens, growing vertically in chains and forming into depth hoar, and 3) micro-cavities developed above the crust creating less ice per unit volume. However, relating these observations to the thermophysical observations was unsuccessful, as no change in the temperature profile was observed to occur near the ice crust. Greene notes that the potential reason was the spatial resolution (1 cm) of the thermocouples or the size of the thermocouple (255 um).

A more recent study was performed by Hammonds et al. (2015) to further investigate the thermophysical properties at a snow-ice interface [23], using more advanced techniques such as micro-CT, sub-millimeter micro-thermocouple measurements and scanning electron microscopy. The sample was created in the laboratory using natural rounded snow grains and housed in a 50 mm tall and 19 mm diameter polycarbonate tube. Manufactured ice lenses of varying sizes (2, 4, and 8 mm) were placed in the middle of the housing, with 2.5-3 mm rounded snow grains above and below. The sample was then placed under a $-100°$C m^{-1} TG and allowed to go to steady-state. The microstructural observations were the same as Greene, but further solidified with these more advanced techniques. The second part of this study involved placing multiple micro-thermocouples within 1 mm above and below the ice lens. During this part of the study, only a 4 mm ice lens was used and the TG was varied (-100, -50, -10, and $-4°$C m^{-1}). The local TG above and below the ice lens was measured to be -300 and $-650°$C m^{-1}, respectively, while the imposed TG was $-100°$C m^{-1} (Figure 2.5). Furthermore, in a concluding analysis [20], it was found that 1) the enhanced TG was primarily due to a thermal contact resistance at the snow-ice interface, 2) the water vapor flux was four times greater near the bottom of the ice lens than the bulk snow, and 3) latent heat contributed less than 10% to the enhanced TG. This study assumes that any temperature change unaccounted for by Equation 2.1 was due to a thermal contact resistance. Although a reasonable assumption, further experiments need to be done to further identify the exact reasons for observing such a large local TG near the ice lens.

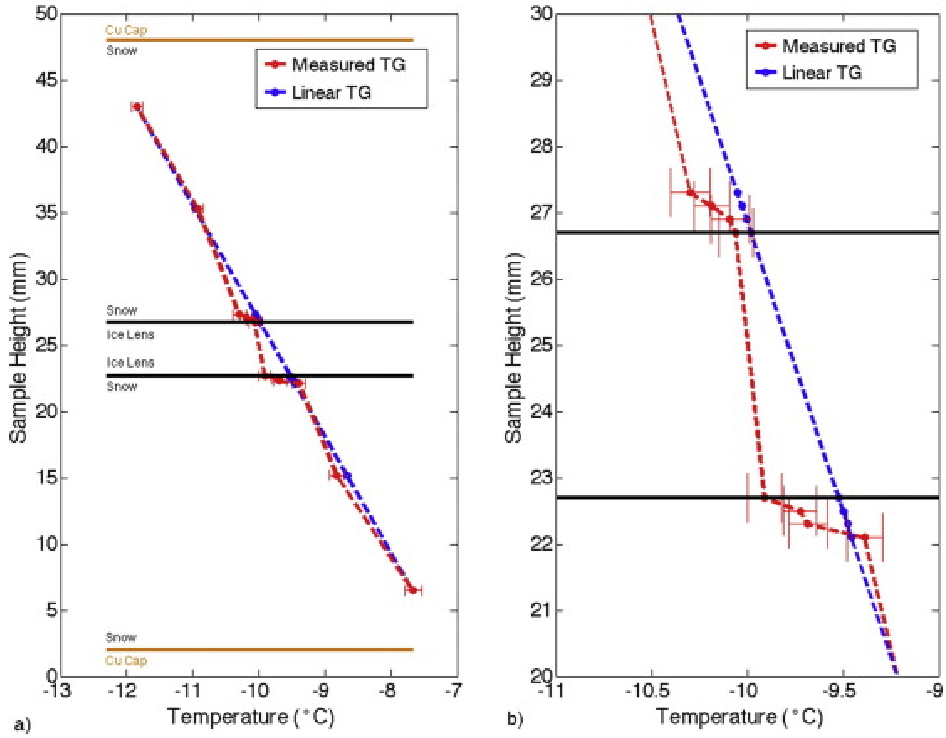

Figure 2.5: Hammonds et el. (2015) TG measurements over the height of a 2.5-3 mm grain size sample with an imposed TG of $-100°\text{C m}^{-1}$ at steady-state (left). The same measurements, but zoomed in to 10 mm around the ice lens (right) [23].

2.5 Research Gap

The change in microstructure observed by Greene (2007) and Hammonds et al. (2015) indicate a faster rate of kinetic snow metamorphism near the interface, which would be a result of a larger TG present. Hammonds et al. (2015) measured the TG within 1 mm of the ice lens and observed TG's much larger than the bulk. After a thermal analysis, the thermal contact resistance was the primary contributor to the overall increase in TG. The limited number of experiments performed provides suspicion of the final measurements, especially with how much error is available to propagate. Along with this, the thermal contact resistance is speculated, because any heat not accounted for by Equation 2.1, is deemed to be from the thermal contact resistance. While this is a good assumption, the system is very complicated and difficult to model. In order to further determine that the enhanced TG is due to a thermal contact resistance, the parameters that effect it must be changed and observed. To do this, the grain size was changed from smaller to larger snow grain, which directly correlates to the amount of contact area between the ice and the snow. The contact area is the primary mechanism for the thermal contact resistance. Therefore, the TG at the snow-ice interface should increase as the imposed grain size increases. This result and more experiments observing the enhanced TG at the snow-ice interface would further solidify the results from Hammonds et al. (2015 & 2016) and a thermal contact resistance at the snow-ice interface.

CHAPTER THREE

METHODS

3.1 Sample Preparation

Snow samples were prepared in a temperature-controlled cold chamber held at $-10°C$. The sample holder consisted of a polycarbonate tube, with dimensions of 17 mm inner diameter, 20 mm outer diameter, and 50 mm in length (Figure 3.1). Polycrystalline ice was made in the laboratory using the same process as Hammonds (2018) [21] and cut with a precision band saw down to a cylindrical disk, with a diameter similar to the outer diameter of the polycarbonate tube (20 mm). Because the ice was cored using the sample holder, it was ensured the ice lens created an impermeable barrier to vapor flow. The lens was then cut on top and bottom to create flat surfaces and a thickness of 4 mm. After placing the lens in the middle of the tube at 25 mm from the end, sieved snow of similar grain size was loaded above and below. The snow was collected from nature but allowed to sinter for >1 year at an isothermal temperature of $-10°C$. The snow grains were well-rounded and then sieved to three different size distributions for each experiment; 0.90-1.12 mm, 1.80-2.24 mm, and 2.80-3.15 mm. These sizes were chosen specifically to narrow down the average grain size to roughly 1, 2, and 3 mm. Moving forward these ranges will be referred to accordingly, however, it is recognized that these are not the exact grain sizes and will fluctuate within the sieved range. Each side was enclosed with press-fit 4 mm thick copper caps, to eliminate any exterior influences and maximize heat transfer through the top and bottom.

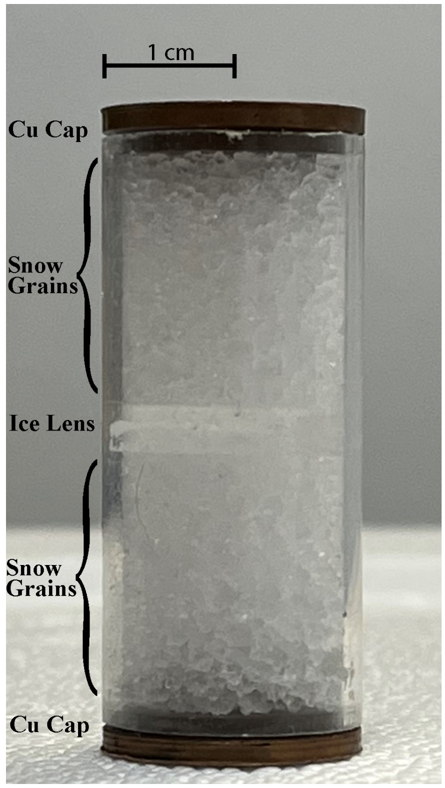

Figure 3.1: Ice lens sample with a 4 mm lens and 2 mm snow grains above and below.

3.2 Temperature Gradient Apparatus

The sample was then placed into a TG apparatus built for these experiments, shown in Figure 3.2, which was housed in a cold room set at −10°C. Polystyrene foam was cut to the housing size and placed around the sample, providing 30 mm of insulation on all sides. Thermoelectric peltier modules (12711-5P31-12CW) were above and below the sample which controls the surface temperature to an accuracy of ±0.1°C. For maximum heat transfer efficiency, they were attached to copper heat sinks using adhesive aluminum (TS-MF3A6). Internal flow channels in the copper blocks create cooling for the hot sides of the peltier modules, which were filled using a glycol chiller, which was held at −10°C ±1°C. A thermistor (TR91-170) was epoxied to each peltier using a resin/aluminum blend to monitor the surface temperature. The peltiers and thermistors were wired to control boards (5R7-573) that monitor and hold the set temperature to an accuracy of ±0.1°C. Each peltier was controlled using software from Oven Industries, which can be fine-tuned for high precision. Once the sample was loaded into the TG apparatus, a TG of $-100°C\ m^{-1}$ was applied by setting the top and bottom peltiers to $-7.7°C$ and $-12.4°C$ respectively.

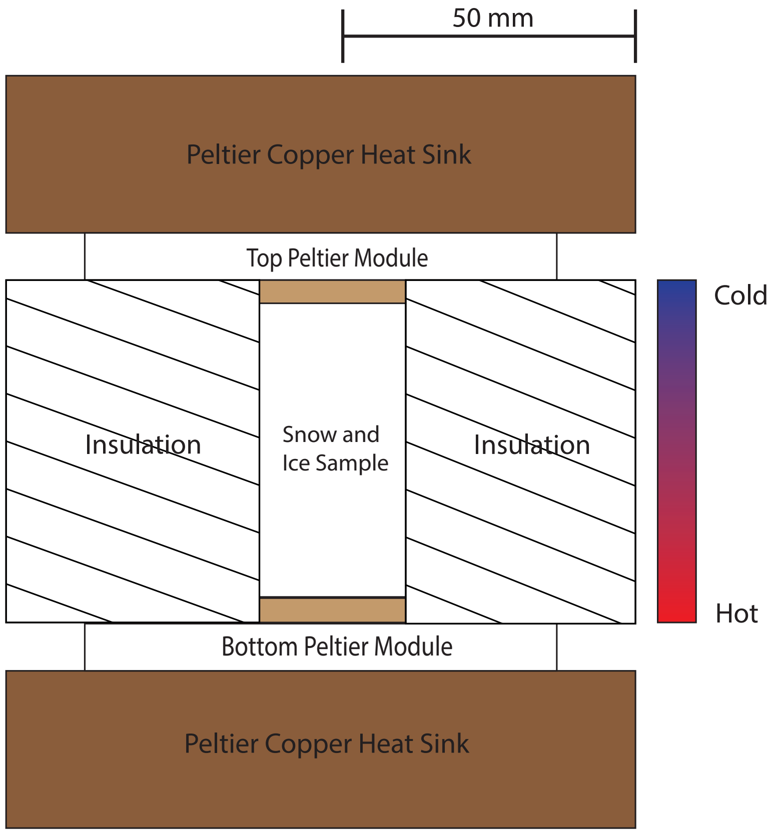

Figure 3.2: Schematic of the TG apparatus used, with a cross-section of the sample loaded. The color bar on the right represents the relative temperature the peltiers were set to, and the subsequent direction of upward heat flow.

3.3 Time-Lapse X-ray Computed Micro-tomography

In a parallel set of experiments, a SkyScan 1173 micro-CT was used for imagery, which was housed in the same room the experiment was conducted, with an ambient temperature of $-10°C$. The sample was scanned every 12H, over 48H, totaling 5 scans which includes a 0H scan. Scans were done using a voltage of 42 kV and current of 190 μA, with a pixel resolution of 15 μm. A scan was taken every 0.7° for a total of 180°. The whole process took approximately 20 minutes. Grayscale images were attained using the software NRecon, where a Gaussian filter, post alignment, and smoothing were applied. The grayscale images were then transferred into another software CTan, which binarised the images. The grayscale image was first filtered using a median 3D filter, then thresholded over a 0-250 scale. Thresholding varied from sample to sample based on scanning conditions, the thresholding value was chosen by selecting the lowest value between the air and ice phase. After thresholding, a black and white despeckle was applied to anything smaller than 25 voxels.

Using the same software, CTan, 3D images and parameters were obtained for different volumes of interest (VOI). The 3D reconstructions viewed the ice lens and 3 mm above and below, with dimensions of 10.5x4.5x10.5 mm and were created using a Double-Time Cubes algorithm. All micro-CT parameters were calculated using a region of interest of a 14 mm diameter circle and 1.5 mm above and below the ice lens. The position of the top and bottom of the ice lens was determined visually. While this method is inherently subjective, the lens is easily seen and the resulting data has no significant fluctuations between time steps, showing that the method is reliable. Two other VOI's were used to observe the snow-ice interface, 0.5 mm below and 0.3 mm above the ice lens, with the same diameter of 14 mm. The values differ because the interface was larger on the bottom than on the top. This is likely due to the settling of snow grains, where they will be more organized at the bottom of a pile than at the top (i.e. top and bottom of the ice lens).

The microstructural parameters that were of interest were, mean intercept length (MIL), connectivity density, SSA, total porosity, and structure model index (SMI) [7]. Each value was derived using CTan.

MIL is found by sending a line through a binarised image and dividing the number of intersections by the length of the line. With a 3D stack of images, a sphere is formed in the VOI and the process is done many times to calculate the MIL in many directions. This method is commonly used to measure the Degree of Anisotropy by looking at how MIL changes in different directions [24]. MIL correlates with object thickness or grain size in a given direction but does not measure it directly. In this study, it was used to estimate the change in the mean grain diameter within a VOI and not to draw conclusions of the exact mean grain diameter.

The connectivity density represents how many connections or nodes per unit volume are present. This is calculated using a Euler analysis to find the number of connection points [41]. This value was then divided by the total volume to get connectivity density, which can indicate the number of bond between snow grains.

The SSA compares how the object surface area changes with respect to the object volume. In other terms it is the ratio of ice surface area and the object volume. The object surface area was calculated by subtracting the intersection surface area from the total surface area which removes the additional area artificially made when creating a VOI [35]. The change in SSA represents a change in free energy and object size, which correlates to surface area and volume respectively.

The total porosity is the ratio of all the pore space and total VOI volume. The pore space volume includes the closed pore space, which is air fully surrounded by ice and the open pore space which is not enclosed by ice. The porosity of snow will increase if the grains are growing in size and decrease if mean grain size decreases, for example, if new crystal growth occurs.

The SMI is calculated using surface area and volume, by dilating the 3D voxel and comparing the dilated surface area to the original parameters [25]. The result of this calculation is similar to the mean curvature used in previous studies that also observed snow

[9]. The mean curvature is a reflection of the average curvature over a VOI. A positive SMI indicates the presence of convex structures such as spheres or rounded snow grains. As SMI increases this would point towards a decrease in grain size or a more rounded microstructure forming. An SMI of zero is a flat structure, meaning that flatter faceted grains can decrease the overall SMI of a VOI. It should be noted that concave surfaces such that are present in firn can also create negative SMI values [30].

3.4 In-situ Micro-Thermocouple Measurements

To measure the TG at a sub-millimeter scale, the same sample housing as Hammonds et al. (2015) was used. The sample housing used for the micro-CT was modified using a high precision milling machine with an accuracy of 10 μm. From Hammonds et al. (2015), the face was square milled to make it flat and a series of 12 holes were drilled with diameters of 360 μm. The holes allow for the placement of Type T Omega Precision Fine Wire Thermocouples with a diameter of 79 μm. After the sample was made, thermocouples were placed at the bottom of each hole and then covered with electrical tape to hold them in place (Figure 3.3). The holes were drilled in a vertical line, except for the eight around the 4 mm ice lens. These were placed in a linear array, to attain 4 measurements within 1 mm above and below the ice lens. This was achieved by vertically staggering the holes by 200 μm for a total distance of 600 μm, measured vertically from the center of the bottom to the top hole. The sample was then loaded into the TG apparatus and placed under a TG. The bottom was held constant at -7.7°C, while the top was first set to -8.1°C and then sequentially stepped down to -10°C and -12.4°C once steady-state was achieved every two hours. These values equate to a TG of -10, -50 and -100°C m^{-1}. The thermocouples were wired to an Agilent 34970A data logger, which sampled every 15 seconds. The data logger reduced measurement noise by using built-in signaling conditioning along with a power line cycle set to 2. The thermocouples were calibrated using an ice bath but needed additional post-calibration due to the uncertainty of the precise location of the thermocouples. This involved removing the sample from the cold room to melt, so the thermocouples would not move in position, then the tube was then reloaded with a homogeneous grain size of 0.92-1.18 mm and no ice lens. The 1 mm grain size was used for all experiments so the grains would not hit and potentially move the thermocouples. The TG's described above were then applied and a linear temperature profile was found by drawing a straight line from the bottom to the top thermocouple. Each measurement between was subtracted over to the linear line and this acted as the calibration for the snow-ice sample previously done. The experiment was repeated seven times for each sample, for a total of 21 experiments.

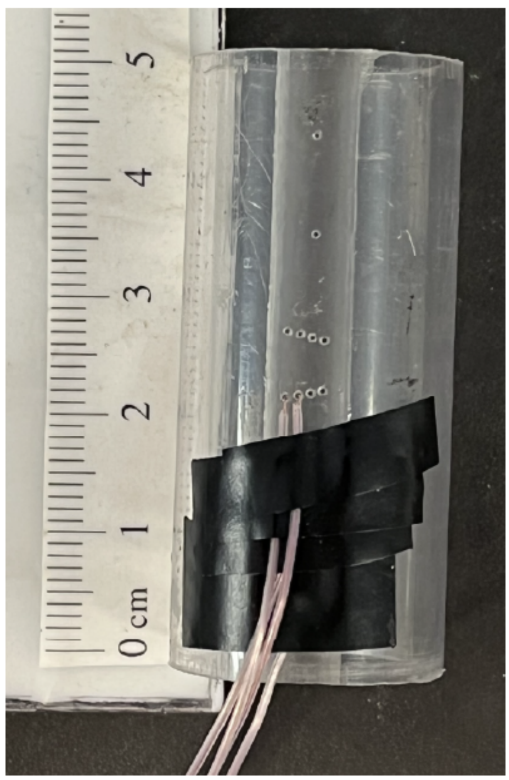

Figure 3.3: Photograph of the sample holder with thermocouple holes and the first four micro-thermocouples inserted. Note that this photo was taken after the sample was melted out and the thermocouples were inserted into the snow sample.

3.5 Thermal Analysis

A thermal analysis was performed utilizing the governing equations described in Section 2.1, to further understand the physical meaning of the measured TG's. This was done by segmenting the temperature measurements into four different regions where R1 and R4 were the bulk measurements below and above the ice lens, R2 and R3 were 0.6 mm below and above the ice lens, capturing the snow-ice interface.

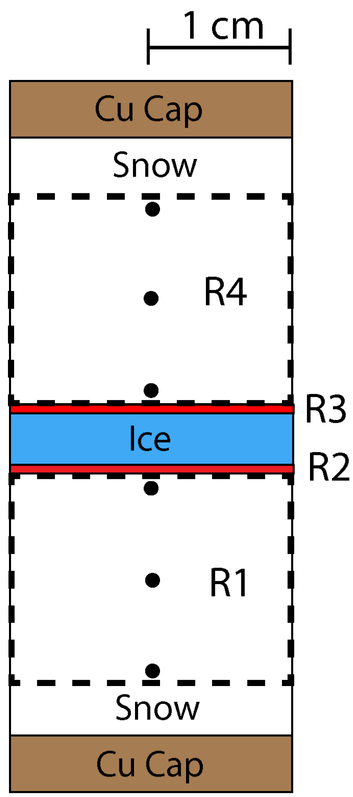

Figure 3.4: Illustration showing the different regions used in the thermal analysis, the black dots represent thermocouple placements in the bulk. Regions 2 and 3 are highlighted in red and are 0.6 mm in height.

The heat flux in R1 was found using Equation 3.1, where $q_{latentheat}$ and $q_{conduction}$ were calculated using Equations 2.2-2.6.

$$Q_{tot} = q_{latentheat} + q_{conduction} \tag{3.1}$$

By satisfying the energy balance across a substrate with steady-state heat flow conditions, it was assumed that the heat flux remained constant across the sample (Q1=Q2=Q3=Q4=Q_{tot}) [28]. The total resistance of R2 and R3 includes the latent heat and conduction terms, with any remaining resistance assumed to be caused by a thermal contact resistance. The thermal contact resistance was calculated using Equation 3.2, where the change in temperature and heat flux from the effects of latent heat were first removed from the totals. Then the resistance due to conduction, R_C, was calculated using Equation 3.3 [5] and also subtracted from the total resistance. The final Matlab code used can be seen in Appendix D.

$$R_{TCR} = \frac{\Delta T - \Delta T_{latentheat}}{Q_{tot} - q_{latentheat}} - R_C \tag{3.2}$$

$$R_C = \frac{L}{k} \tag{3.3}$$

Hammonds and Baker (2016) performed a similar analysis as the one described above. However, there were adjustments made due to the fact that many samples were done and inconsistencies between experiments arose. Hammonds (2016) calculated Q_{tot} using the temperature difference across the ice, which is a good method if the thermocouples are in contact with the ice. However, if the thermocouples are not, then the temperature difference would change due to not measuring via conduction against the ice, which was observed when analyzing multiple samples. This is why Q_{tot} was derived by solving for Q1 using the derived k_{eff} (Eq. 2.3), which provided more consistent results. The other difference between the two analyses, was how the linear TG was calculated, Hammonds (2015) considered the peltier surface temperature to be the temperature at the bottom and top of the copper caps. Whereas I used the bottom and top temperature measurements in the snow via an ice bath calibration. This method allowed for a more accurate linear TG measurement due to the direct temperature measurements in the snow.

CHAPTER FOUR

RESULTS

4.1 Micro-CT Observations

Observations from the micro-CT generally reflect the results from Hammonds (2015) and Greene (2007). Each sample had new ice crystal growth on the bottom of the ice lens, while the top of the lens sublimated away. Kinetic snow metamorphism was also observed as the rounded snow grains decreased in size, while also becoming more angular and faceted. The wave-like structure on the top of the ice lens that Hammonds (2015) observed, was also be seen at 48 hours in Figure 4.1.

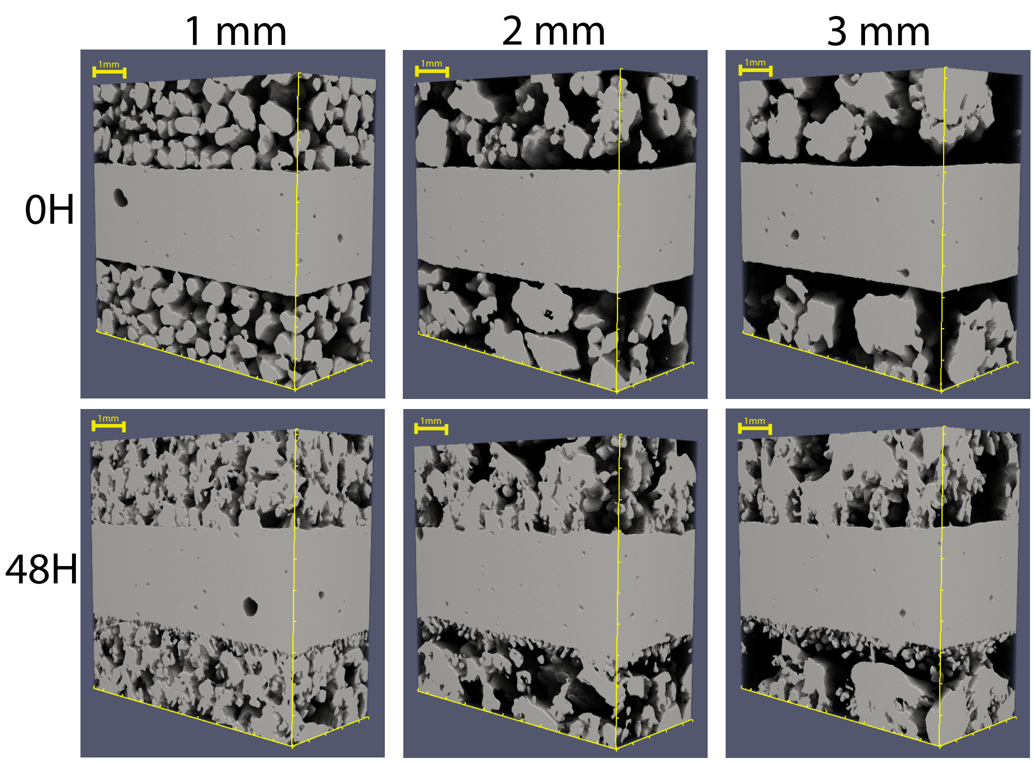

Figure 4.1: Initial and final three-dimensional reconstructions of 1, 2, and 3 mm samples under a constant $-100°C\ m^{-1}$ TG.

Above the ice lens, as shown in Figure 4.1, the snow grains appear to grow into the ice lens. This observation is likely due to the large amounts of water vapor being released from the surface of the ice and depositing onto the grains above. The 2 and 3 mm reconstructions distinctly show the process of sublimation and deposition, with the top of the grain being smooth and the bottom more rough. The direct comparison from 0H to 48H should be avoided because the exact snow grains were not captured in each reconstruction. The 0H images show the difference in contact points between the varying grain sizes at the snow-ice interface. Notably, as the grain size increases, the number of contact points decreases. The VOI remains constant between all grain sizes and the number of grains reduces as the grain size increases and a larger pore space is subsequently present. Below the ice lens, the size of new crystal growth increases in vertical length as grain size increase (left to right).

Based on Figure 4.1 the vapor deposition below the ice lens appears to be rounded. However, Figure 4.2 shows the orthogonal 2D grayscale images, which exhibit grains with sharp corners representing a kinetic growth regime. This distinction between the two occurs when an image is smoothed during 3D reconstruction. The 2D representation (Figure 4.2) exhibits a change in the width of the new crystal growth size below the ice, and becomes larger as the grain size increase. The large grains in the 1 mm case should not be mistaken as new crystal growth, the snow-ice interface is so small that there is overlap into the 2D cross-section, encompassing the bulk snow grains. The visible striations at 48 hours in Figure 4.2, were similarly observed by Hammonds (2015) and were formed by the band saw during sample preparation. New ice crystal growth preferentially formed on the ridges created by the band saw. Clusters of grain growth below the lens were also observed, which are attributed to larger amounts of water vapor available, (i.e. snow-ice contact points). Above the lens, there were faceted structures that appear to be fragmented due to the large amounts of water vapor sublimating from the ice lens. The 2D and 3D observations indicate faceting and new crystal growth at the snow-ice interface. While these processes can be observed visually, microstructural parameterization allows for a further understanding of the magnitude and rates at which they occur.

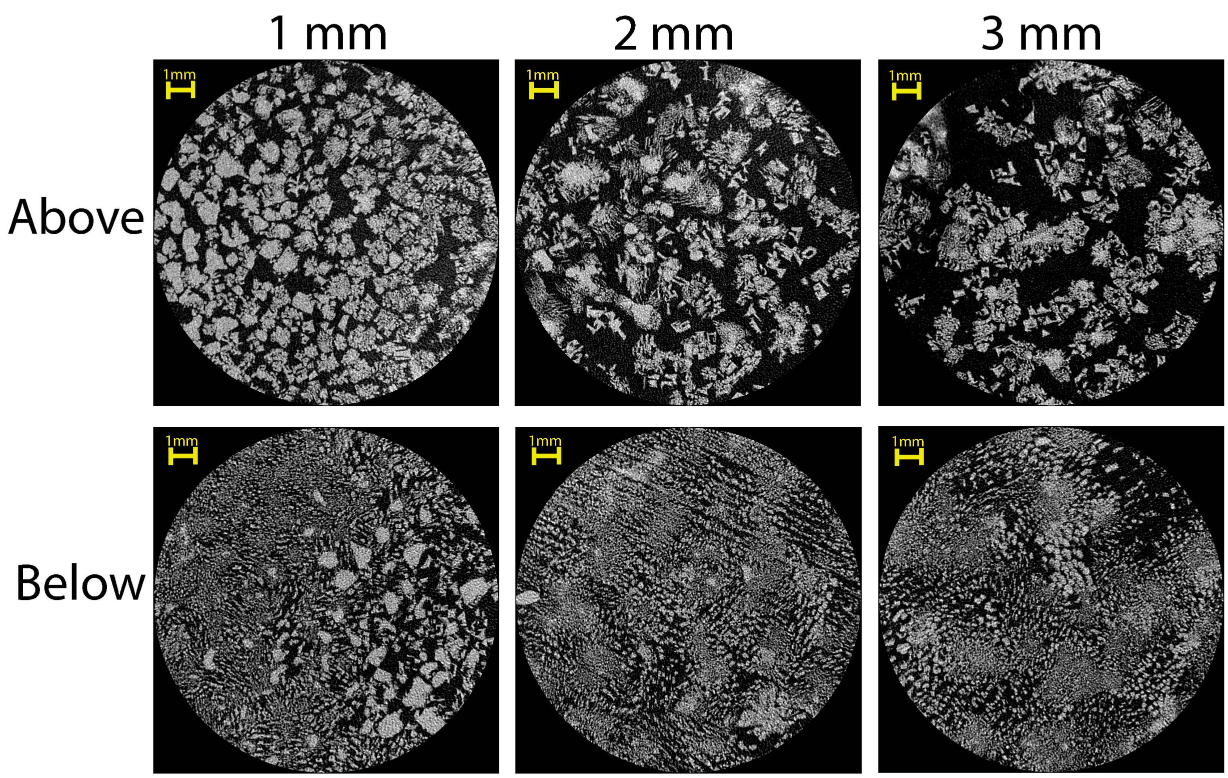

Figure 4.2: Two-dimensional grayscale images that are perpendicular to the direction of heat flow and immediately above and below the ice lens. This is after the sample has been exposed to the $-100°C\ m^{-1}$ TG for 48 hours.

4.2 Micro-CT Analysis

4.2.1 Mean Intercept Length (MIL)

The MIL values shown in Figure 4.3 were calculated over the larger VOI of 1.5 mm in height above and below the ice lens. The solid and dashed lines are the best linear fits via least squares fitting to the data points. Figure 4.3a shows how the raw MIL data does not correlate directly to grain diameter, however, the decreasing trend indicates a decrease in mean grain diameter over time. All of the grain sizes have a more rapid decrease below the ice lens than above, which was also observed by Hammonds (2015). The faster decrease is attributed to the new ice crystal growth on the bottom of the ice lens. With respect to the overall decreasing trend, I believe this is due to the rounded grains undergoing kinetic snow metamorphism. The values in Figure 4.3b were normalized by using Equation 4.1, which forces all of the data points to begin at 1 and change with respect to the initial data point. The normalization provides a comparison for the growth rates between grain sizes.

$$Normalized = \frac{y_i}{y_1} \tag{4.1}$$

Using the normalized MIL (Figure 4.3b), it is clear that as the grain size increases, the negative rate also increases. The difference between the 2 and 3 mm cases are not as drastic as 1 and 2mm, which is likely due to the pore size allowing for more new ice crystal growth to occur. As the pore size increase, there would be more space for the new ice crystals to grow. This can be visually seen in Figure 4.1, where the new crystal growth merges with the rounded snow grains in the 1 mm case. Alternatively, the growth is independent of the rounded grains and larger in the 2 and 3 mm cases.

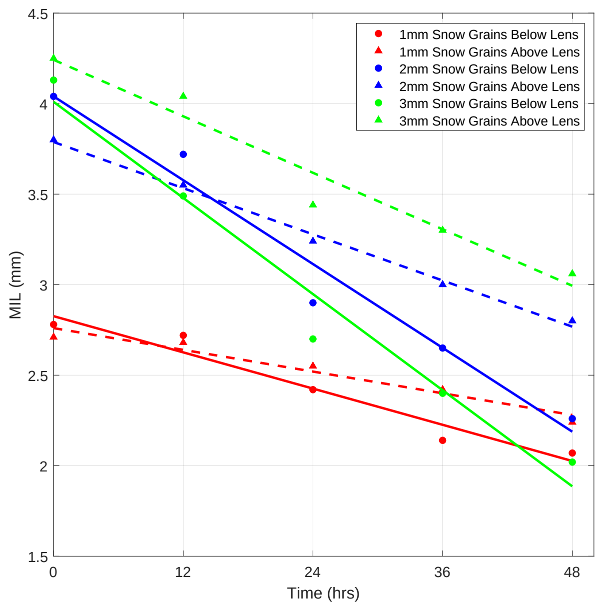

(a) MIL time-series

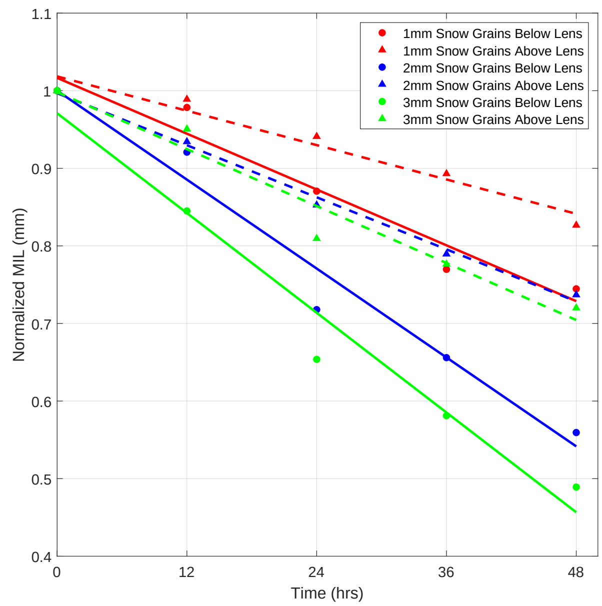

(b) MIL normalized

Figure 4.3: Evolution of mean intercept length over 48H and a constant $-100°\mathrm{C}\ \mathrm{m}^{-1}$ TG applied. The same 1.5 mm VOI was used for all grain sizes, also above (Dashed) and below (Solid) the ice lens.

4.2.2 Connectivity Density

Connectivity density represents the number of connections per unit volume (Section 3.3). The same VOI size as the MIL was used for all data points. At 0H, the 1 mm case has more connections than the 2 and 3 mm cases (Figure 4.4a). Just as MIL, the connectivity density of the 2 mm case is only slightly larger than the 3 mm case, if not at all. This may also be some function of porosity, or potentially the VOI is not large enough to encapsulate a difference. More importantly, the rate of change is shown by the normalized connectivity density (Figure 4.4b), which was calculated the same way as the normalized MIL using Equation 4.1. The connectivity density results agree with Hammonds (2015) where the bottom increases faster than the top due to new crystal growth. The change in connectivity with respect to grain size is consistent with observations presented above, as the

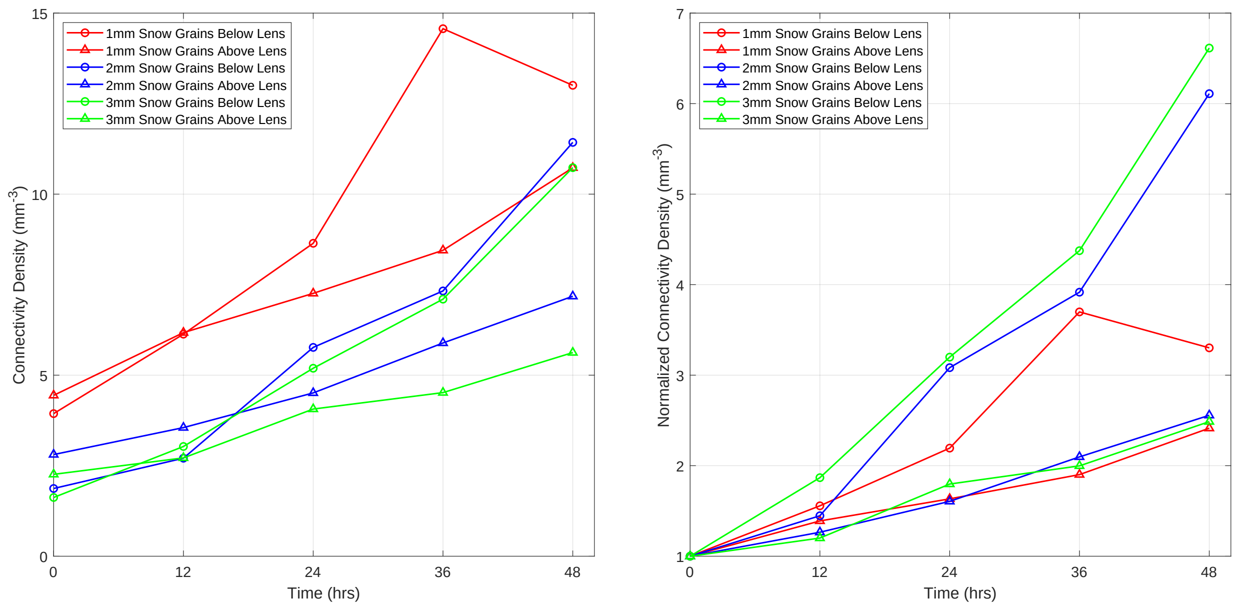

(a) Connectivity Density (b) Normalized Connectivity Density

Figure 4.4: Evolution of Connectivity Density over 48H and a constant $-100°$C m^{-1} temperature gradient applied. The same VOI was used for all grain sizes.

grain size increases, so does the connectivity density (i.e. new crystal growth). The increase in connections should not be mistaken with an increase in mechanical strength or snow grain bonds, as one would have to account for the change in microstructure. It is unclear why the connectivity density begins to decrease in the 1 mm case below the ice at 48 H. This could be due to the new crystal growth reaching the larger snow grains, and preferentially growing. The grain size has less of an effect above the ice lens because the vapor supply released from the ice lens is constant throughout grain sizes. The water vapor flux from the top ice surface should be constant because the top surface of the ice experiences the same TG and surface area.

4.2.3 Specific Surface Area

When computing SSA, the previous VOI's of 1.5 mm tall were used, with the addition of smaller VOI's to capture the interfacial region. The determined size was was due to the size of the interface, 0.5 mm below and 0.3 mm above the ice lens were chosen. The difference in the interface size is because the bottom interface is larger than the top due to the way that spheres pack next to each other [20]. By modeling snow grains as spheres, they would pack more efficiently on top of a surface (ice lens) and become more disorganized as they move up. At 0H the grain sizes start near the same SSA value, and then begin to increase with time (Figure 4.5). In the 1.5 mm VOI, the SSA increases slightly which indicates both a larger surface area and a change in microstructure, rounded to facets. The bottom is influenced by the new crystal growth, which has a larger amount of surface area compared to its volume and increases slightly faster than above the lens. The SSA of the interface VOI above the ice lens increases at a faster rate than the large VOI, which becomes more enhanced as grain size increases. A significant trend occurs in the interface VOI below the ice lens and is contradictory to Hammonds (2015). This is because they used a dynamic binning approach that attempted to track the crystal growth region, whereas I used a fixed 0.5 mm region to capture the overall change. Hammonds (2015) shows SSA decreasing, which is likely due to the introduction of large rounded grains as they move away from the ice lens. Instead, it was observed here that SSA was increasing as a result of small angular crystals forming on the bottom of the ice lens (Figure 4.5). The SSA peaked at approximately 24H or 36H, depending on the grain size case and then remained relatively constant. The SSA peak became larger and more rapid as the grain size increased, indicating faster ice crystal growth with larger snow grain sizes. Each grain size case has a unique inflection point where the SSA rate of change begins to decrease. This is interpreted as the new crystals reaching a critical size in which the volume begins to increase as fast as the surface area, indicating that the new crystals are growing in size.

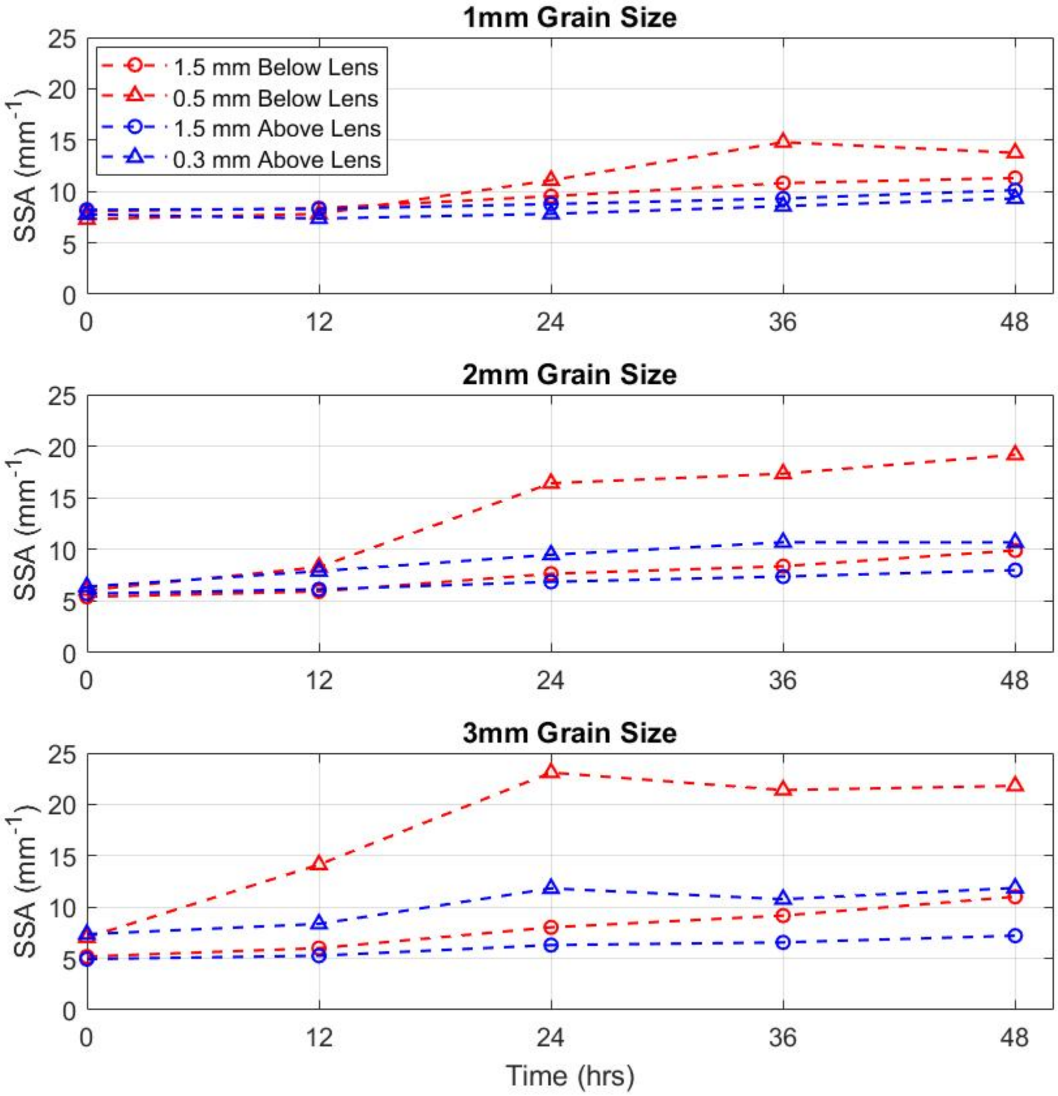

Figure 4.5: SSA for the 1, 2, and 3 mm cases while under a constant $-100°\text{C m}^{-1}$ TG over 48H. The dashed blue and red lines indicate VOI's above and below the ice lens, respectively. The VOI height is then distinguished by circles and triangles.

4.2.4 Porosity

The porosity was calculated using the same VOI's as SSA (Figure 4.6). All porosity values in the large VOI begin within 5% of each other. The 1 mm case has nearly the same porosity across all regions, the difference between the interface and large VOI then increases with grain size. The increasing difference shows the impact of the grain's ability to organize better above the lens than below and how smaller grains can pack closer together. The porosity slightly decreased above the lens due to the water vapor from the ice lens. Below the lens, the porosity in the 1 mm case remained unchanged. The porosity in the 2 and 3 mm cases increased slightly before peaking. This increase is likely due to initial crystal growth on the ice lens that was not captured by the micro-CT. This trend is consistent with the interface VOI below the lens and represents the new crystal growth. The rates of declining porosity after the peak correlate with the grain size; with a larger grain size corresponding to a faster decrease in porosity. The interface VOI above the lens consistently decreases at a faster rate than the larger VOI above the lens, which also has increasing rates with larger grain sizes. Observing the initial porosity of the large VOI's (circles) and interface VOI's (triangles) shows how the grain size affects the size of the interface. The 3 mm grain size nearly has a difference of 20% whereas the 1 mm has little to no difference. This change in porosity is thought to have significant implications for the thermal behavior, discussed in Section 5.

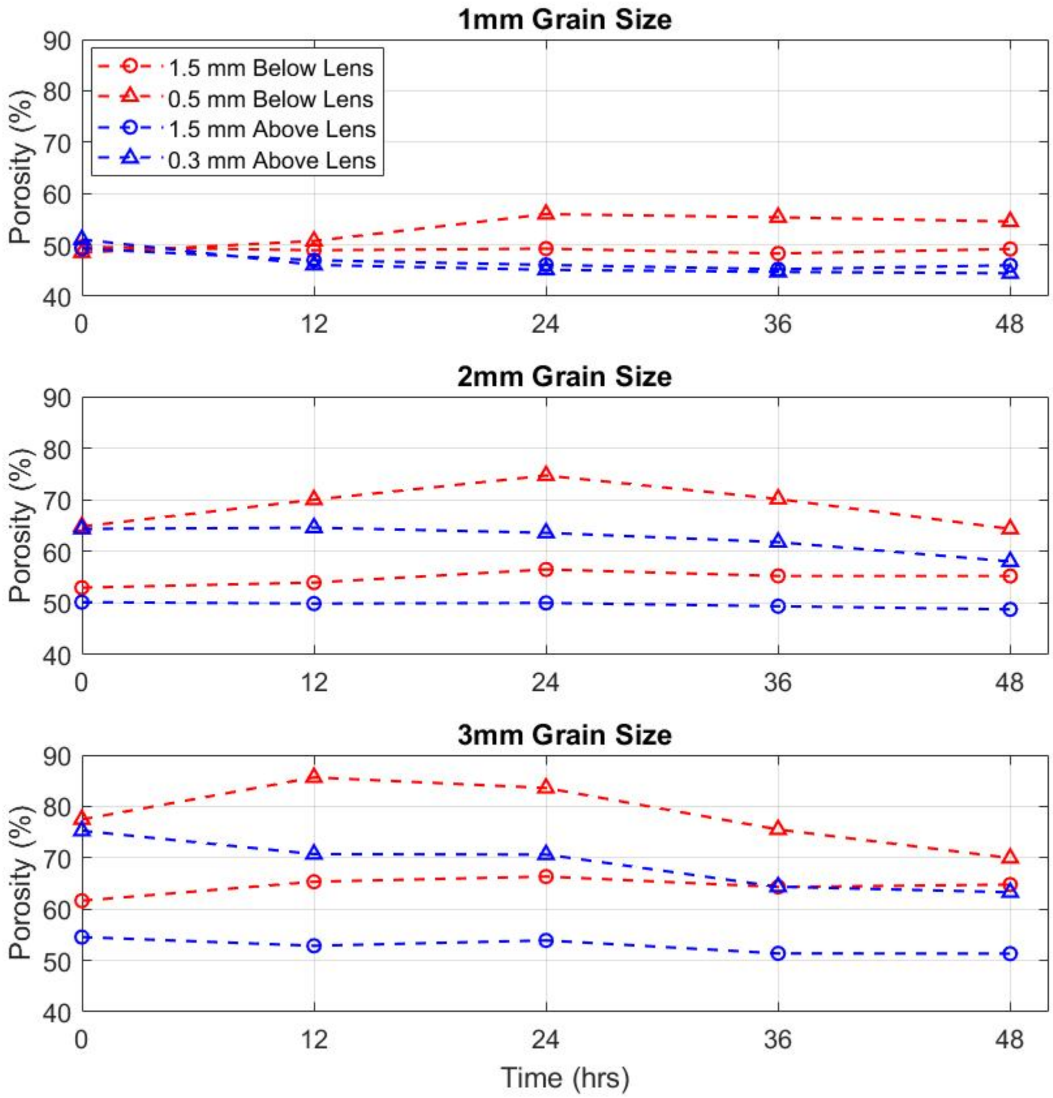

Figure 4.6: Porosity for the 1, 2, and 3 mm cases while under a constant $-100°C\ m^{-1}$ TG over 48H. The dashed blue and red lines indicate VOI's above and below the ice lens, respectively. The VOI height is then distinguished by circles and triangles.

4.2.5 Structure Model Index

The SMI was evaluated over the two larger VOI's, with the interface VOI's being excluded. When comparing SMI values between different VOI's it is not reliable to make conclusions due to the methods used to calculate SMI. However, comparing the same VOI over time is consistent and can be compared. Figure 4.7 shows what a change in SMI indicates about the microstructural change from the initial rounded snow grains. The SMI is shown in Figure 4.8, which decreases above the lens, indicating a faceted structure is forming. No significant differences can be drawn between grain sizes. However, below the ice lens trends vary between grain sizes. The 2 and 3 mm cases initially increase, indicating a decrease in mean grain size. SMI then goes down at 24H, showing that the grains are beginning to grow and/or become faceted. The 1 mm case fluctuates but does not deviate significantly from the initial value. The SMI ends at a lower point, also indicating faceted structures or a decreasing grain size. The grain size influences the magnitude of the SMI increase and rate, being that it increases more and faster with larger grain sizes.

SMI Increase:	Decrease in mean grain diameter		
SMI Decrease:	Increase in mean grain diameter	OR	Faceted structure is forming

Figure 4.7: A matrix indicating how a change in SMI should effect rounded snow grains.

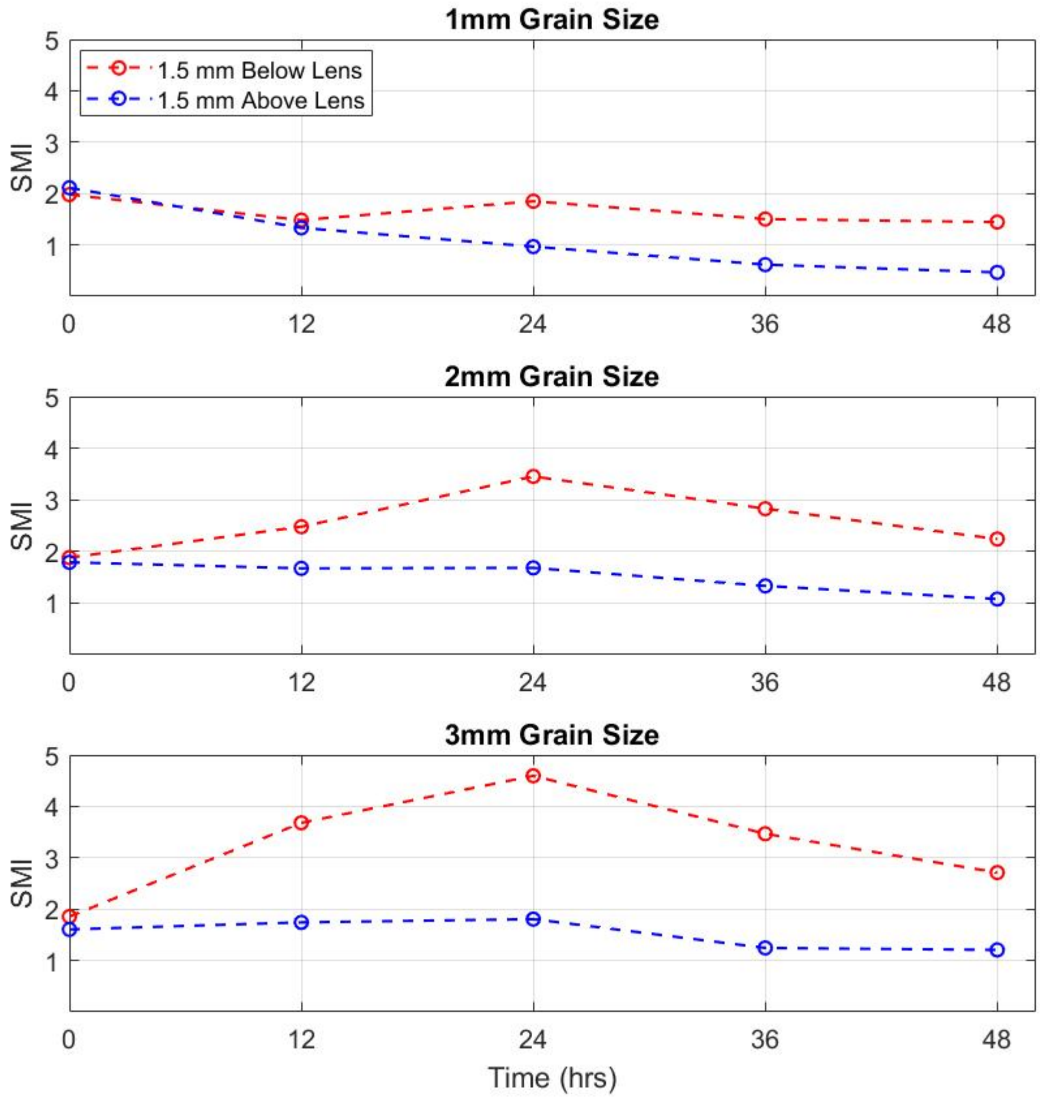

Figure 4.8: SMI for the 1, 2 and 3 mm cases while under a constant $-100°\mathrm{C}\ \mathrm{m}^{-1}$ TG over 48H. The dashed blue and red lines indicate VOI's above and below the ice lens, respectively.

4.3 Micro-thermocouple Measurements

After the calibration process was completed, 200 temperature measurements at steady-state were averaged for each thermocouple. A $-10°C\ m^{-1}$ and 2 mm grain size case is shown in Figure 4.9. The red dashed line follows the measured temperature measurements, whereas the dashed blue line connects the first and last measurements. The dashed blue line represents the linear TG that would be expected to occur in a one-dimensional homogeneous sample. The error bars were calculated using a standard error calculation (Equation 4.2), where σ is the standard deviation and n is the sample size. Equation 4.2 will be the method to calculate the error bars for all future plots.

$$SE = \frac{\sigma}{\sqrt{n}} \tag{4.2}$$

Figure 4.9 shows a typical trend, where the temperature at the bottom and top deviate from the linear TG (blue line). The steep line across the ice lens shows how well ice can transport heat rather than snow due to its much larger thermal conductivity.

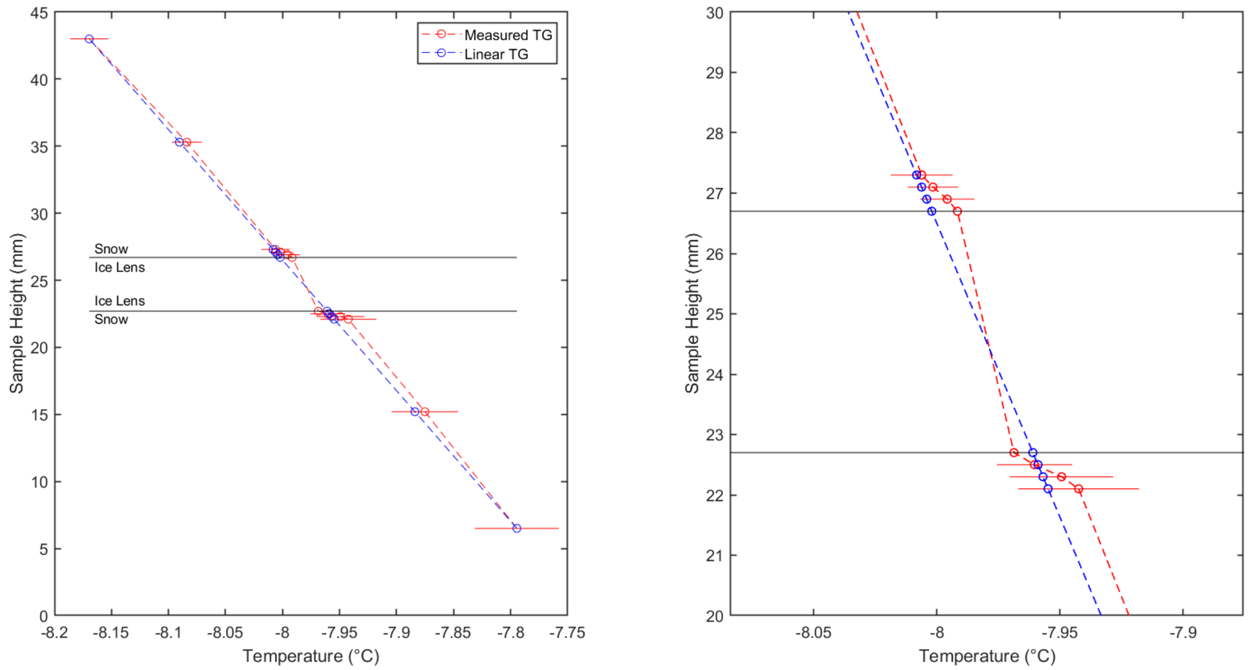

Figure 4.9: TG measurements over the height of a 2 mm grain size sample with an imposed TG of $-10°\text{C m}^{-1}$ at steady-state (left). The same measurements, but zoomed in to 10 mm around the ice lens (right)

The temperature data from each experiment were then fitted by a least squares method to calculate the linear TG in four different regions. The regions were described in Section 3.5, and correlate to the four temperature measurements immediately above and below the lens and the two on top and bottom for the bulk TG. Several TG's above or below were larger than zero due to the inherent error of the thermocouple placement, which is later discussed in Chapter 5. This was deemed as a nonphysical process based on the fundamental equations discussed in Chapter 2. The unreasonable nature of the positive TG data is based on the fact that the bottom of the sample is warmer than the top, which then defines flow of heat as moving in the vertical direction. Neither of the terms from the total heat flux (Q_{tot}), comprising of conduction and latent heat would reverse the heat flow and create a positive TG. This is why any positive TG's were removed from the final results. The percentage of data removed from the final result can be seen in Figure 4.10. The positive TG label represents the individual data points that were removed from each case due to a positive TG. The 1 and 2 mm cases have relatively low percentages of about 4%, whereas the 3 mm case is more than double. The larger amounts of error in the 3 mm case is further discussed throughout the rest of the thesis. The largest amount of error is from removing entire experiments due to the large amount of scatter observed. This is likely due to the thermocouples moving during the calibration process.

<table>
<tr><th>Grain Size</th><th>Positive TG</th></tr>
<tr><td>1 mm</td><td>3.2%</td></tr>
<tr><td>2 mm</td><td>4.0%</td></tr>
<tr><td>3 mm</td><td>8.7%</td></tr>
<tr><td colspan="2">Entire experiments removed</td></tr>
<tr><td colspan="2">28.50%</td></tr>
</table>

Figure 4.10: The amount of data removed from the final data set. The positive TG column is when a positive TG was observed. While the entire experiments removed column is a removal of a data set due to large amounts of scatter in the data.

An example is shown in Figure 4.11, which is a 1 mm sample under a $-50°\mathrm{C}\ \mathrm{m}^{-1}$ TG. However, half of the temperature data directly above the ice lens shifts and trends in the positive direction. This is thought to be a result of random error,most likely due to the thermocouples shifting during the calibration process and an example of why that TG data point was removed. All of the data collected using the methods presented above can be seen in Appendix C.

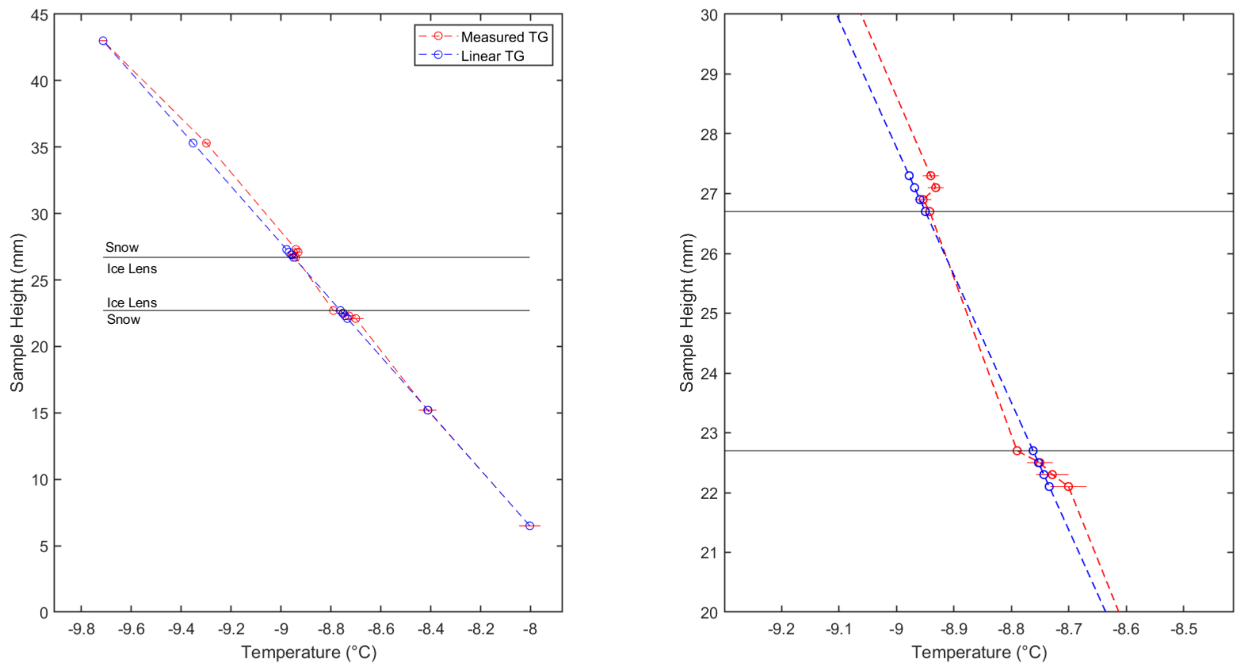

Figure 4.11: TG measurements over the height of a 1 mm grain size sample with an imposed TG of $-50°C\ m^{-1}$ at steady-state (left). The same measurements, but zoomed in to 10 mm around the ice lens (right). This is an example of error and an outlier above the ice lens.

The result of averaging all TG measurements over the three imposed TG's -10, -50, and $-100°C\ m^{-1}$ is shown in Figure 4.12. The measured bulk TG was within $\pm 5°C\ m^{-1}$ of the theoretical TG, but was more consistent between each experiment at around $\pm 1°\ m^{-1}$. Below the ice lens is consistent between each imposed TG, with the 1 mm case near the bulk TG and drastically increased with grain size. The inflection point that decreases from 2 to 3 mm is not an expected result. I attribute it to a large experimental error that occurs with such coarse grain sizes and will be further discussed in Chapter 5. The rest of the plots in the results section also have the inflection due to their dependence on the TG. I will not be addressing it in the future plots due to the redundancy and issue will be discussed in Chapter 5. Generally, above the ice lens has a TG similar to that of the bulk. However, the $-10°C\ m^{-1}$ case shown in Figure 4.12a indicates an increasing trend with grain size, similar to the trend below the ice lens. This is likely due to the large amounts of water vapor flux sublimating off the ice lens at such high TG's. This concept will be further discussed in Chapter 5.

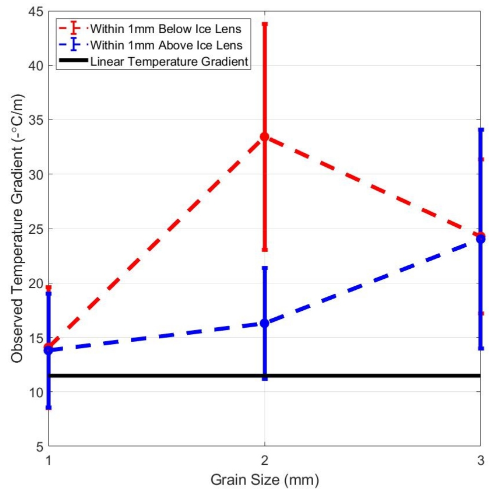

(a) $-10°\text{C m}^{-1}$ Imposed TG

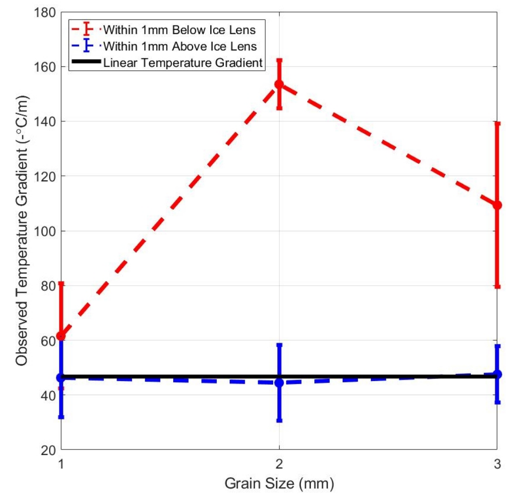

(b) $-50°\text{C m}^{-1}$ Imposed TG

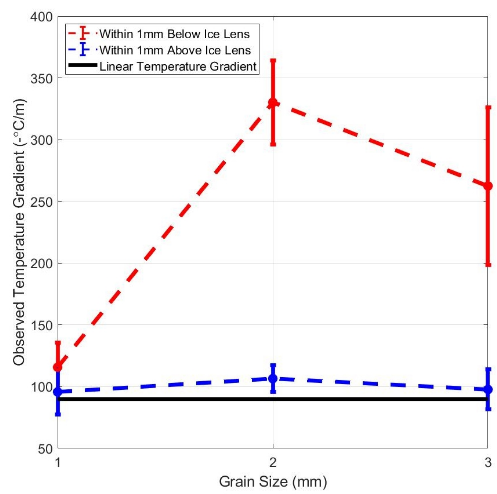

(c) $-100°\text{C m}^{-1}$ Imposed TG

Figure 4.12: The average TG measured over multiple experiments, each grouped by the imposed TG 4.12a, 4.12b, 4.12c.

4.4 Temperature Gradient Analysis

4.4.1 Water Vapor Flux

In calculating the water vapor flux (J_z), the same approach was used as Hammonds & Baker (2016) and Pinzer et al. (2012), using Equations 2.5 and 2.6. The results are shown in Figure 4.13 and have a similar trend as the observed TG (Figure 4.12). The similarities are due to the dependence that the water vapor flux has on the TG. The large flux below the lens would explain the new crystal growth seen in Figures 4.2 and 4.1. It would also explain why the new ice crystal growth would be faceted because of the large supersaturation inducing kinetic growth. The vapor flux above the lens is not as large but may have higher consequences for mechanical stability, depending on the thickness and cohesion of the ice crust. Overall, the large vapor flux in these areas creates conditions for an increased rate of kinetic snow metamorphism.

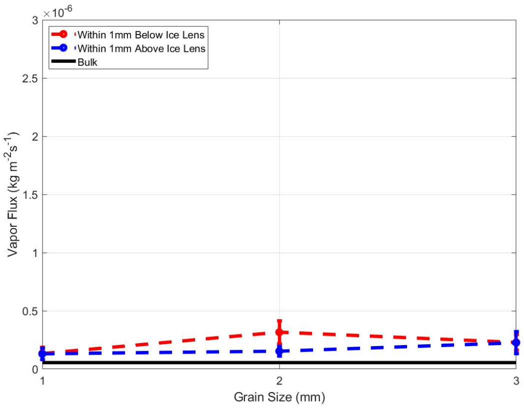

(a) $-10°$C m^{-1} Imposed TG

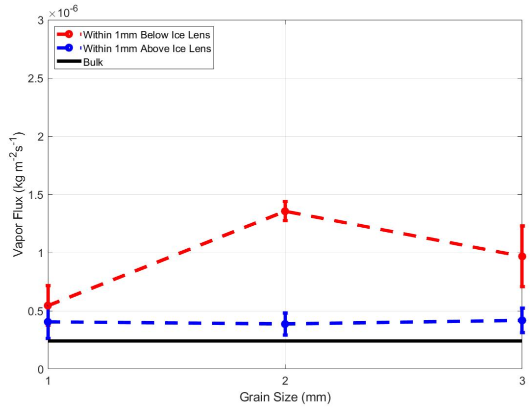

(b) $-50°$C m^{-1} Imposed TG

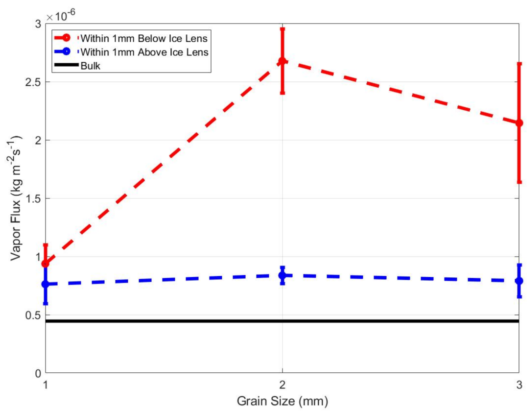

(c) $-100°$C m^{-1} Imposed TG

Figure 4.13: The average vapor flux calculated over multiple experiments, each grouped by the imposed TG 4.13a, 4.13b, 4.13c.

4.4.2 Temperature Gradient Contribution

The latent heat was calculated using Equation 2.4, then evaluated as a percentage over the entire heat flux in each region. Figure 4.14 compares the contribution that each mode of heat transport added to the overall change in temperature and subsequently heat flux. The contribution due to conduction is not included because it is less important than its counterparts. The contribution from conduction is the rest of the heat flux adding to 100%.

The values for the latent heat flux are not displayed because it is linearly dependent on the water vapor flux and has the same trend (Figure 4.13). Latent heat is released below the ice lens due to the deposition of the new ice crystals on the bottom surface of the ice. However, it is unclear how much is released into the pore space or if it is absorbed by the ice. Hammonds (2016) observed minor amounts of "bread-loafing" on the new crystal growth, which would signify heat being released into the pore space. Realistically it is most likely a function of the conditions present and a combination of the two. Above the lens, the latent heat transfer is not restricted by the conductive capacity because of the sublimation off the surface of the ice. This effect would decrease the temperature at the surface of the ice, and would counteract any thermal contact resistance present, reducing ΔT. This is potentially the reason why an enhanced TG was not seen in the -50 and -100°C m^{-1} cases above the ice (Figure 4.12). Whereas in the -10°C m^{-1} case the observed TG increases with grain size, which is the same trend as the bottom of the ice. The transition as the imposed TG decreases, may be due to a decreasing amount of sublimation off the surface of the ice and in turn less able to counteract the thermal contact resistance that is present.

The contribution to the heat flux from the release of latent heat is between 5% and 20% depending on the case observed. The contribution from a thermal contact resistance has a similar trend to the observed TG (Figure 4.12), exhibiting an increase in contribution and grain size. Below the ice lens, the thermal contact resistance begins at around 20% in the 1 mm case and increases up to 55% at 2 mm as less contact area is available. The latent heat increases from 5% to 20% in the 1 mm and 2 mm cases, due to the large TG present. Above the lens, there is still a presence of a thermal contact resistance near 10% in the -50 and -100°C m^{-1}. The -10°C m^{-1} case increases as the grain size increases, which also follows the observed TG trend. The latent heat follows a similar trend between all of the imposed TG's, but remains below 10%.

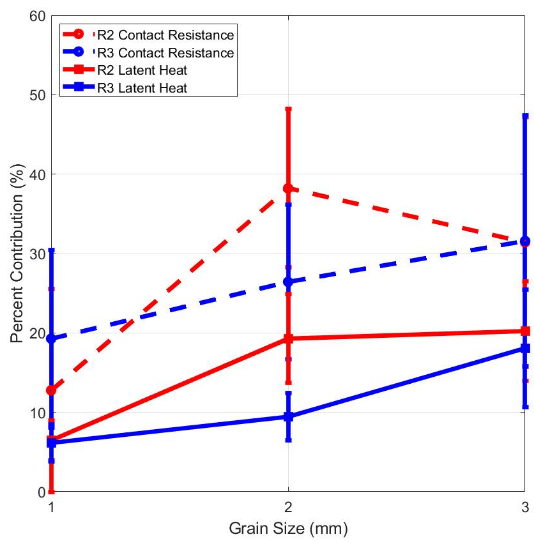

(a) $-10°C\ m^{-1}$ Imposed TG

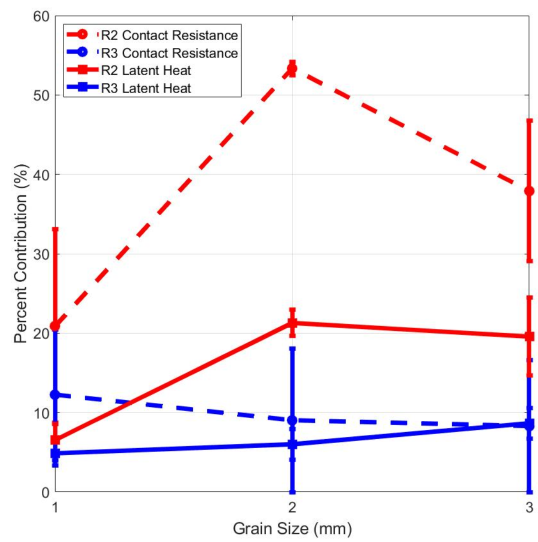

(b) $-50°C\ m^{-1}$ Imposed TG

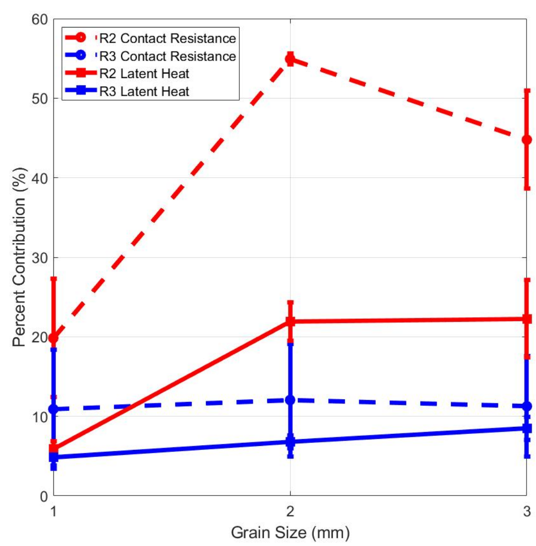

(c) $-100°C\ m^{-1}$ Imposed TG

Figure 4.14: The contribution of each mode of heat transfer contributed to total heat flux calculated over multiple experiments and each grouped by the imposed TG 4.14a, 4.14b, 4.14c.

CHAPTER FIVE

DISCUSSION

5.1 Thermal Contact Resistance

The TG average over each grain size and TG case shown in Figure 4.12 suggests that there are thermal discontinuities at a snow-ice interface. Based on the analysis in Section 4.4, I attribute this to a thermal contact resistance between the snow and ice. Based on our calculations, the thermal contact resistance can contribute up to 55% depending on the grain size present. There was an enhanced TG below the ice lens over all of the TG's imposed onto each sample. However, this varied with respect to the snow grain size, with the 1 mm case remaining near the bulk TG, and as the grain size increased, so did the observed TG. There was a decline in the observed TG from the 2 to 3 mm case, shown in Figure 4.12. This result was unexpected. Based on micro-CT data, the microstructural effects at the ice lens only become more enhanced as the grain size increased. Because of the micro-CT data and fundamental equations discussed in Section 2, I would expect this value to also increase. The inflection of the TG's between 2 and 3 mm could be a result of some change in heat transfer, potentially due to convection because of such a high TG present. However, it is more likely due to the large pore size within the 3 mm grain samples, compared to the thermocouple's small diameter and spacing. The values from the 3 mm case were quite varied and inconsistent, which is shown by the large error bars in Figure 4.12 and seen in Appendix C. Measuring the TG over 0.6 mm is most likely influenced by the position of the thermocouple in comparison to the pore space or grain. It is thought that having too much variability in this large of a grain size would introduce significant amounts of error. Figure 5.1 is a good representation of how this would occur in such a coarse grain size. The middle thermocouples are sitting in the pore space, whereas the ones on the edges sit against the ice and snow. Thermocouples perform better when in contact with a solid material with a higher thermal conductivity such as ice [1]. When measuring the air temperature in the pore space, there is a minor amount of error that is introduced. While minor, any error can have large implications for the small temperature measurements made in this study.

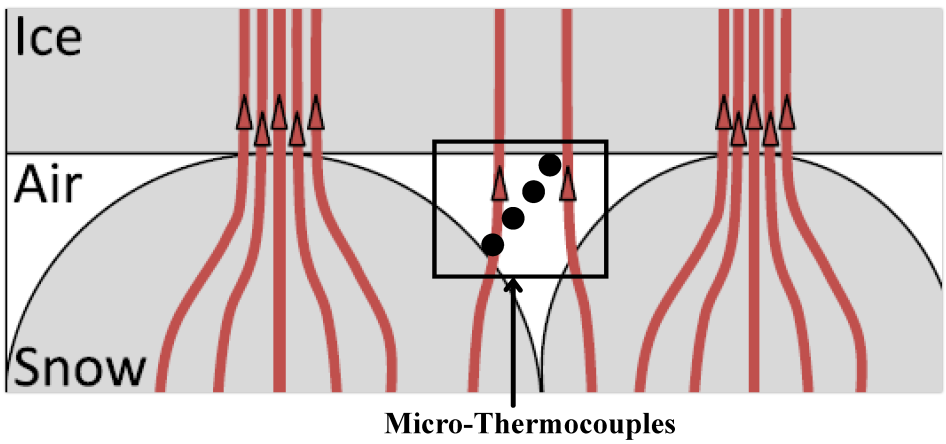

Figure 5.1: Two snow grains of 3 mm in size against an ice lens and the micro-thermocouple array shown as black dots. The red lines represent heat flow paths, which preferentially flow through the snow-ice interface [23].

5.2 Latent Heat

The observed TG above the ice lens followed the bulk TG relatively close with the $-10°\text{C m}^{-1}$ case being an exception. The trend that the $-10°\text{C m}^{-1}$ case exhibited is the more expected result, which follows the TG trend below the ice lens. I believe that this is due to the latent heat flux from the surface of the ice lens. It was observed that the surface of the ice lens became smooth and wave-like from the micro-CT reconstruction and scanning electron microscopy imagery done by Hammonds (2016). The result of latent heat being sublimated at the ice surface would lead to a colder surface and a warmer temperature some distance above where vapor deposition occurs onto a snow grain. This would have consequences for an enhancement of the TG, by bringing the thermocouple measurements above the lens in Figure 4.9 closer together. Bringing the measurements closer together would reduce steady-state ΔT above the ice lens and subsequently the TG. If this were the case, it would explain why the observed TG above the ice remains near the bulk for the high TG's of -50 and -100°C m^{-1}. Whereas the -10°C m^{-1} has significantly less vapor flux (Figure 4.13) and latent heat absorbed at the top ice surface.

5.3 Temperature Gradient Multiplier

Overall, the observed TG at the snow-ice interface became larger as the grain size increased, with the caveat of the error at the 3 mm grain size case. This is indicative of a thermal contact resistance, because of the reduced contact area between the snow and ice needed for conduction to occur. The reduced contact area can be observed visually in Figure 4.1 and numerically from the differences in the porosity at the interface vs. the bulk (Figure 4.6). To compare how the observed TG diverged from the bulk TG, I took a similar approach to Hammonds (2015) by classifying a temperature gradient multiplier (TGM) shown in Equation 5.1.

$$TGM = \frac{ObservedTemperatureGradient}{ImposedTemperatureGradient} \tag{5.1}$$

The results are shown in Figure 5.2, which demonstrate how within each grain size case the TGM increased slightly below the ice lens over the different imposed TG's. The increase could be due to a couple of reasons, 1) An increase in water vapor flux and latent heat released into the pore space, 2) A larger amount of heat must be moved through the interface. I suspect that the latter explanation is correct, but it is unclear exactly which is the driving mechanism. However, utilizing finite element software or a modeling technique could help to further distinguish the primary factors.

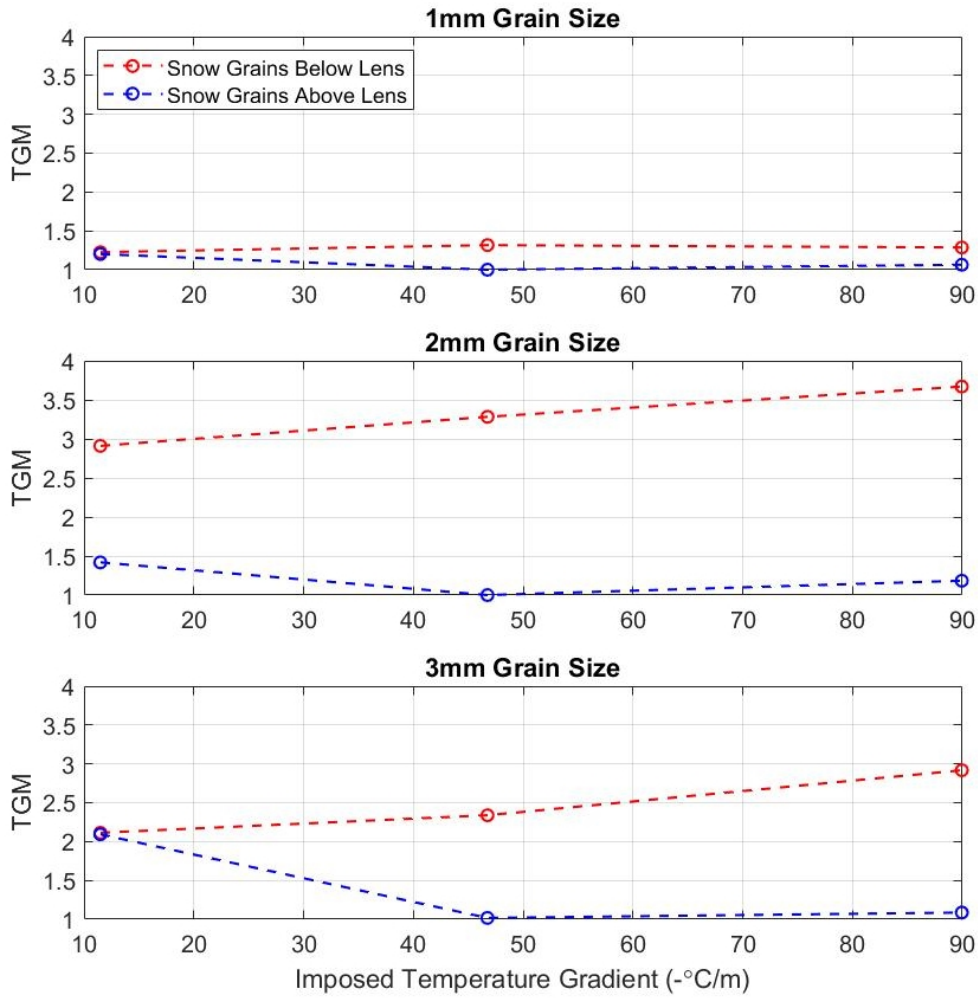

Figure 5.2: The temperature gradient multiplier above and below the ice lens for all temperature and grain size cases.

5.4 Comparison to Previous Work

The micro-CT provided informative data that was similar to previous work. Both Green (2007) and Hammonds (2015) observed new ice crystal growth below an ice lens and sublimation on the top surface of the ice lens. One difference between Hammonds (2015) and this study was the micro-CT parameters for new ice crystal growth. Hammonds had a dynamic binning scheme that increased the size of the VOI to track the growth, which lead to a decreasing SSA. We fixed our binning to 0.5 mm below the ice lens and observed the SSA increasing as new ice crystals grew. We believe this difference is due to the introduction of large rounded grains to the VOI as Hammonds moved away from the ice lens. Large rounded grains have a much lower SSA and would subsequently decrease the SSA as more were introduced.

The only previous temperature measurements at a sub-millimeter scale near a snow-ice interface were by Hammonds (2015). They found TG's as large as -650 and -300°C m^{-1} below and above the ice lens, respectively, using a 2.5-3 mm grain size and an imposed TG of -100°C m^{-1}. We would expect to see similar values if the trend had continued past the 2 mm grain size. However, I was unsuccessful at consistently measuring the 3 mm grain size. This could be due to Hammonds (2015) used a wider range of grain sizes (0.5 mm) compared to our 0.35 mm range. They may have avoided the error seen in the 3 mm case by reducing the grain size and increasing the range, allowing for the grains to pack more efficiently in the pore space. Hammonds results combined with micro-CT data, further solidify that the trend seen from the 1-2 mm case should continue to increase as the grain size increases. It is unclear why Hammonds observed such a large TG above the ice lens and I did not. A large difference seen is that Hammonds found the TGM increased a factor of 6, from 6 to 40 times as the imposed TG declined, whereas ours had a minor decrease of 1.25 times. This could be due to a difference in the calibration process, however, I am confident in my methods.

5.5 Uncertainty of Temperature Measurements

Although I saw repeatable results, it should be recognized that there was uncertainty in each measurement. The systematic error was quite low due to the tedious calibration process. The systematic error is presented in the error bars of each temperature measurement in Figure 4.9, which reflects the variation of temperature at steady-state. The random error is larger and could not be controlled. Below is the recognized random error:

1. Placement of thermocouples
   - Thermocouple was not placed at the bottom of the hole
   - Thermocouple inserts at an angle
2. Position of thermocouple with respect to snow grains.
3. Thermocouples moving during melting phase of calibration

Although the error above was present, multiple samples were measured and the random error was calculated via the standard error of the mean. We deem the results significant due to small standard error values and results that can be explained by thermophysical processes.

CHAPTER SIX

CONCLUSION

Two parallel sets of snow samples were made, one for micro-CT analysis and one for in-situ temperature measurements. The samples were created using three different sieve ranges that were near the grain sizes of 1, 2, and 3 mm. A 4 mm ice lens was placed between each of the snow grain sizes and the sample was subjected to a controlled temperature gradient of $-100°\text{C m}^{-1}$. The samples were then analyzed using time-lapse computed X-ray micro-tomography over 48 hours. Micro-thermocouples were then inserted each experiment, with 200 μm spacing and subjected to various temperature gradients of -10, -50, and $-100°\text{C m}^{-1}$. The temperature gradient was measured at a sub-millimeter scale above and below the ice lens over multiple samples. Following these experiments, a thermal analysis was done to further understand the mechanisms of heat transfer and the effect on the snow microstructure. I found that:

i. Large snow grains (2-3 mm) near an ice lens increase the local temperature gradient by up to 4 times the imposed temperature gradient.

ii. The temperature gradient multiplier increases with the imposed temperature gradient with a 2-3 mm grain size present below the ice lens by a factor of 25%.

iii. The thermal contact resistance at a snow-ice interface is the primary contributor to the change in temperature across the interface, with the contribution below the ice lens being as high as 55% in the 2 mm grain size.

iv. Large amounts of water vapor flux (Imposed TG $\geq -50°\text{C m}^{-1}$) may counteract the thermal contact resistance above the ice lens, due to the effects of latent heat exchanged near the interface.

Although I found significant results pointing towards a thermal contact resistance, a mass and heat transfer model would be useful for further delineating the contributing factors. The next step would be to apply the same methods to field samples and observe the temperature distribution of naturally formed permeable ice crusts.

REFERENCES CITED

[1] Acromag. Criteria for temperature sensor selection of t/c and rtd sensor types, 2011.

[2] EE Adams and RL Brown. Metamorphism of dry snow as a result of temperature gradient and vapor density differences. *Annals of Glaciology*, 4:3–9, 1983.

[3] EE Adams and RL Brown. A mixture theory for evaluating heat and mass transport processes in nonhomogeneous snow. *Continuum Mechanics and Thermodynamics*, 2(1):31–63, 1990.

[4] Eizi Akitaya. Studies on depth hoar. *Contributions from the Institute of Low Temperature Science*, 26:1–67, 1974.

[5] Theodore L Bergman, Frank P Incropera, David P DeWitt, and Adrienne S Lavine. *Fundamentals of heat and mass transfer*. John Wiley & Sons, 2011.

[6] Karl W Birkeland, Ron F Johnson, and D Scott Schmidt. Near-surface faceted crystals formed by diurnal recrystallization: A case study of weak layer formation in the mountain snowpack and its contribution to snow avalanches. *Arctic and Alpine Research*, 30(2):200–204, 1998.

[7] Bruker. Morphometric parameters measured by skyscan ct-analyser software, 2009.

[8] N. Calonne, F. Flin, S. Morin, B. Lesaffre, S. Rolland du Roscoat, and C. Geindreau. Numerical and experimental investigations of the effective thermal conductivity of snow. *Geophysical Research Letters*, 38(23), 2011.

[9] Neige Calonne, Frédéric Flin, Christian Geindreau, Bernard Lesaffre, and S Rolland du Roscoat. Study of a temperature gradient metamorphism of snow from 3-d images: time evolution of microstructures, physical properties and their associated anisotropy. *The Cryosphere*, 8(6):2255–2274, 2014.

[10] S. C. Colbeck. Theory of metamorphism of dry snow. *Journal of Geophysical Research: Oceans*, 88(C9):5475–5482, 1983.

[11] Samuel C Colbeck. An overview of seasonal snow metamorphism. *Reviews of Geophysics*, 20(1):45–61, 1982.

[12] Samuel C Colbeck. A review of sintering in seasonal snow. 1997.

[13] Samuel C Colbeck and J Bruce Jamieson. The formation of faceted layers above crusts. *Cold Regions Science and Technology*, 33(2-3):247–252, 2001.

[14] Charles Fierz. Field observation and modelling of weak-layer evolution. *Annals of Glaciology*, 26:7–13, 1998.

[15] Charles Fierz, Richard L Armstrong, Yves Durand, Pierre Etchevers, Ethan Greene, David M McClung, Kouichi Nishimura, Pramod K Satyawali, and Sergey A Sokratov. The international classification for seasonal snow on the ground. *Tech. Doc. Hydrol.*, 2009.

[16] Kévin Fourteau, Florent Domine, and Pascal Hagenmuller. Impact of water vapor diffusion and latent heat on the effective thermal conductivity of snow. *The Cryosphere*, 15(6):2739–2755, 2021.

[17] Kévin Fourteau, Florent Domine, and Pascal Hagenmuller. Macroscopic water vapor diffusion is not enhanced in snow. *The Cryosphere*, 15(1):389–406, 2021.

[18] Ethan Greene and Greg Johnson. Characterization of a deep slab instability. In *Proceedings ISSW*, pages 491–498, 2002.

[19] Ethan M. Greene. *The thermophysical and microstructural effects of an artificial ice layer in natural snow under kinetic growth metamorphism*. PhD thesis, Colorado State University, January 2007.

[20] Kevin Hammonds and Ian Baker. Investigating the thermophysical properties of the ice–snow interface under a controlled temperature gradient part ii: Analysis. *Cold Regions Science and Technology*, 125:12–20, 2016.

[21] Kevin Hammonds and Ian Baker. The effects of h2so4 on the mechanical behavior and microstructural evolution of polycrystalline ice. *Journal of Geophysical Research: Earth Surface*, 123(3):535–556, 2018.

[22] Kevin Hammonds and Ethan Greene. Leave your thermometer at home… but don't forget your loupe! *The Avalanche Review*, 35:22–23, 2016.

[23] Kevin Hammonds, Ross Lieb-Lappen, Ian Baker, and Xuan Wang. Investigating the thermophysical properties of the ice–snow interface under a controlled temperature gradient: Part i: Experiments & observations. *Cold Regions Science and Technology*, 120:157–167, 2015.

[24] TP Harrigan and RW Mann. Characterization of microstructural anisotropy in orthotropic materials using a second rank tensor. *Journal of Materials Science*, 19(3):761–767, 1984.

[25] TOR Hildebrand and Peter Rüegsegger. Quantification of bone microarchitecture with the structure model index. *Computer Methods in Biomechanics and Bio Medical Engineering*, 1(1):15–23, 1997.

[26] Bruce Jamieson, Torsten Geldsetzer, and Chris Stethem. Forecasting for deep slab avalanches. *Cold Regions Science and Technology*, 33(2-3):275–290, 2001.

[27] Th U Kaempfer and M Schneebeli. Observation of isothermal metamorphism of new snow and interpretation as a sintering process. *Journal of Geophysical Research: Atmospheres*, 112(D24), 2007.

[28] S Kakaç and Y Yener. Convective heat transfer. communication crc. press, 1993.

[29] Edward R LaChapelle and Richard L Armstrong. Temperature patterns in an alpine snow cover and their influence on snow metamorphism. Technical report, COLORADO UNIV BOULDER INST OF ARCTIC AND ALPINE RESEARCH, 1977.

[30] Yuan Li and Ian Baker. Dynamic observations of the densification of polar firn under compression using a micro-computed tomograph. *Journal of Geophysical Research: Earth Surface*, 126(10):e2021JF006290, 2021.

[31] DM McClung. Avalanche character and fatalities in the high mountains of asia. *Annals of Glaciology*, 57(71):114–118, 2016.

[32] DA Miller and EE Adams. A microstructural dry-snow metamorphism model for kinetic crystal growth. *Journal of Glaciology*, 55(194):1003–1011, 2009.

[33] D. M. Murphy and T. Koop. Review of the vapour pressures of ice and supercooled water for atmospheric applications. *Quarterly Journal of the Royal Meteorological Society*, 131(608):1539–1565, 2005.

[34] BR Pinzer, M Schneebeli, and TU Kaempfer. Vapor flux and recrystallization during dry snow metamorphism under a steady temperature gradient as observed by time-lapse micro-tomography. *The Cryosphere*, 6(5):1141–1155, 2012.

[35] William K Pratt. *Introduction to digital image processing*. CRC press, 2013.

[36] Louis Quéno, Charles Fierz, Alec van Herwijnen, Dylan Longridge, and Nander Wever. Deep ice layer formation in an alpine snowpack: monitoring and modeling. *The Cryosphere*, 14(10):3449–3464, 2020.

[37] Louis Quéno, Vincent Vionnet, Frédéric Cabot, Dominique Vrécourt, and Ingrid Dombrowski-Etchevers. Forecasting and modelling ice layer formation on the snowpack due to freezing precipitation in the pyrenees. *Cold Regions Science and Technology*, 146:19–31, 2018.

[38] F Riche and M Schneebeli. Thermal conductivity of snow measured by three independent methods and anisotropy considerations. *The Cryosphere*, 7(1):217–227, 2013.

[39] E Sadeghi, S Hsieh, and M Bahrami. Thermal conductivity and contact resistance of metal foams. *Journal of Physics D: Applied Physics*, 44(12):125406, 2011.

[40] Shinji Takarada, Tadahide Ui, and Yuko Yamamoto. Depositional features and transportation mechanism of valley-filling iwasegawa and kaida debris avalanches, japan. *Bulletin of Volcanology*, 60(7):508–522, 1999.

[41] Hilde Vermeirsch, Ria Biermans, Philip L Salmon, and Theo F Meert. Evaluation of pain behavior and bone destruction in two arthritic models in guinea pig and rat. *Pharmacology Biochemistry and Behavior*, 87(3):349–359, 2007.

[42] Xuan Wang and Ian Baker. Evolution of the specific surface area of snow during high-temperature gradient metamorphism. *Journal of Geophysical Research: Atmospheres*, 119(24):13–690, 2014.

[43] Zyungo Yosida et al. Physical studies on deposited snow.; thermal properties. *Contributions from the Institute of Low Temperature Science*, 7:19–74, 1955.

APPENDICES

APPENDIX A

EVOLUTION OF EXPERIMENTAL METHODS

To acquire the data presented above, many hurdles and developments had to be made over my two years at Montana State University. The idea for the research began simply by continuing Hammonds (2015) work and applying it to a wind slab interface. However, a new method was to be employed to measure the temperature gradient utilizing micro-electromechanical systems (MEMS). This method was appealing because the position of each thermocouple is fixed relative to the next, removing significant amounts of error with respect to position. Unfortunately, at the time the technology was being developed and the sputtered gold that measured the temperature was flaking off and breaking frequently. Along with this, the calibration process was not reliable and still being defined. Although they did not work initially, after my experience with temperature measurements and the recent developments made in that field, I would go back to this method, attempting to use MEMS. After the recent developments made in MEMS, I believe that one could achieve better data than shown above. Following the troubles presented by MEMS, I resorted to similar methods as Hammonds (2015), utilizing micro-thermocouples. After analyzing micro-CT data of the wind-slab interface, it was determined that the microstructure of the two snow types was too similar and a more distinct interface was desired. If one wanted to investigate a wind slab, I would suggest using 2-3 mm snow grains as the other side of the interface. The next effort was a high density snow created using compression, with low density snow above it. After attempting to accurately define the interface with micro-CT imagery and mean curvature techniques, this approach was also dropped. We finally decided on further investigating the initial snow-ice interface, which was the more obvious choice before moving into more difficult interfaces.

The largest hurdle overall was dealing with suboptimal results and then continuing to run experiments. Many times I got bogged down by not having the result I wanted and stopped in my tracks to change something. I think I would have gotten much further if I would have just kept running experiments, which is eventually what I did in the end. The first adaptation I attempted was 3D printing a similar thermocouple sample holder as Hammonds (2015), which was somewhat successful. But when I didn't get the results I wanted, I scrapped it and used Hammonds sample holder. I now realize that 3D printing is the preferred design, because of the hole placement precision and smaller thermocouple holes that can be created. When designing the sample holder, I would recommend having the length be convenient to cut the ice on a band saw. For example, Hammonds sample holder was the perfect length to use the guide that comes with the band saw, allowing for a near perfect cut. Before running any experiments, ensure the peltier modules are working properly. This is done by measuring the resistance of the peltier and making sure they are near the manufacturing specifications. I would also recommend testing a homogeneous snow sample using ice bath calibrated thermocouples and ensure that results are near the linear temperature gradient. This is a sanity and systems check, if the measurements deviate from the linear temperature gradient, then you are most likely losing heat somewhere, or the peltiers are malfunctioning. Do not worry if the submillimeter measurements are slightly off because they will be! The temperature of the glycol chiller will affect the way that the peltiers perform and introduce different temperatures. I would not worry about this, set it to a reasonable temperature (not too cold, I did $-10°$C) and keep it there for all experiments.

I spent a lot of time trying to understand this, but the matter of fact is that the conditions you apply will not be perfect. However, if you keep the settings the same, you should not introduce any systematic error.

The next issue that consumed my time was the temperature measurements. First off, don't rely on the ice bath calibration of the thermocouples, they need to all be relative to each other and it will not be precise enough. Just keep the ice calibration for the first and last thermocouple for a linear temperature gradient. When making thermocouple measurements, ensure you are using the highest precision data acquisition system (DAQ) you can find with a 6 digit readout. It is also helpful for the DAQ to have noise cancellation because the micro-thermocouples can act as an antenna, consequently picking up signals from the environment. First, make sure no cables or wires are running near the thermocouple wires. Next, don't have the fine micro-thermocouple wire blow in the wind from the evaporators, vibration also induces noise. Lastly, try and make your thermocouple extension wire as short as possible. While all of this is minor amounts of error, it can add up and you will need all the accuracy that you can get.

Finally, the calibration technique is an important step to achieving accurate results. First of all, don't pull the thermocouples out of the snow, melt the snow and then pull them out. If you do not do this you will break all of your thermocouples. I believe that most of the error that occurred was from the snow shifting during the melt out and moving the thermocouples. When melting, ensure that the sample is flat with the thermocouples facing upwards. I used a metal weight with a notch in it that I kept at $-10°C$ in the lab which held the sample well, was flat and did not touch the table surface. I noticed that if the sample touched the warm table surface, that the snow at the bottom would melt fast and create a conical shape allowing the sample to shift or tilt, potentially moving the thermocouples. If the bottom is cold, then the sample will melt from top to bottom, exposing the thermocouples first. At the end of the day, I would decide on a reliable method and run at least 5 samples to see where the data takes you and then go from there. Don't think you will find a magic bullet leading you to success, this is arduous and tedious work.

APPENDIX B

REFERENCED EQUATIONS

$$e = \exp 9.550426 - \frac{5723.265}{T} + 3.53068 \ln T - 0.00728332T \tag{B.1}$$

The equilibrium vapor pressure e (Pa) as a function of T (K) from Murphy and Koop (2005) and also used in Riche & Schneebli (2013) and Hammonds (2016). This is a numerical solution to the Clapeyron equation using a Runge-Kutta method and a constraint at the triple point of water.

APPENDIX C

TEMPERATURE GRADIENT TABLES

Table C.1: Measured temperature gradients of all 1mm samples above the ice lens.

	-10 C/m	-50 C/m	-100 C/m
Sample 1	-10.723	-40.512	-80.588
Sample 2	-0.3274	-64.217	-74.866
Sample 3	3.2836	-27.449	-113.58
Sample 4	-23.018	-91.21	-157.62
Sample 5	-21.136	-8.1212	-51.967
Sample 6	-17.243	-65.03	-108.33
Sample 7	16.454	65.653	108.44

Table C.2: Measured temperature gradients of all 1mm samples below the ice lens.

	-10 C/m	-50 C/m	-100 C/m
Sample 1	-8.7571	-29.293	-59.989
Sample 2	-7.9774	-86.067	-133.82
Sample 3	-8.8664	14.451	42.475
Sample 4	-30.718	-102.51	-116.22
Sample 5	13.914	-28.321	-152.92
Sample 6	-50.743	-207.78	-389.18
Sample 7	-58.646	-259.1	-553.21

Table C.3: Measured temperature gradients of all 2mm samples above the ice lens.

	-10 C/m	-50 C/m	-100 C/m
Sample 1	0.26712	13.478	53.839
Sample 2	-1.6295	-44.591	-107.58
Sample 3	-24.832	-20.491	-87.311
Sample 4	-20.994	-68.325	-124.57
Sample 5	-17.736	43.072	102.58
Sample 6	-24.622	-26.966	-6.6904
Sample 7	4.0493	30.963	78.736

Table C.4: Measured temperature gradients of all 2mm samples below the ice lens.

	-10 C/m	-50 C/m	-100 C/m
Sample 1	-6.3329	-145.07	-326.66
Sample 2	-42.629	-161.44	-263.38
Sample 3	-21.482	-126.09	-265.41
Sample 4	-29.044	-155.98	-450.27
Sample 5	-67.686	-178.83	-345.12
Sample 6	-44.922	-163.77	-434.24
Sample 7	-5.6007	-5.087	195.14

Table C.5: Measured temperature gradients of all 3mm samples above the ice lens.

	-10 C/m	-50 C/m	-100 C/m
Sample 1	-3.9432	-77.547	-124.73
Sample 2	34.838	31.814	39.306
Sample 3	3.4459	-29.907	-68.667
Sample 4	-32.668	-40.069	3.013
Sample 5	-35.488	-42.675	-99.668
Sample 6	-16.886	-10.762	18.445
Sample 7	-12.943	-13.536	-31.655

Table C.6: Measured temperature gradients of all 3mm samples below the ice lens.

	-10 C/m	-50 C/m	-100 C/m
Sample 1	-34.143	-100.6	-280.08
Sample 2	-28.112	-164.79	-363.14
Sample 3	20.396	31.343	38.783
Sample 4	-10.568	-62.619	-144.19
Sample 5	12.112	8.2747	73.082
Sample 6	11.614	-8.5123	-8.9548
Sample 7	-12.843	22.814	31.895

Table C.7: Measured temperature gradients of 1mm samples above the ice lens with outliers removed.

	-10 C/m	-50 C/m	-100 C/m
Sample 1	-10.723	-40.512	-80.588
Sample 2	-0.3274	-64.217	-74.866
Sample 3	NaN	-27.449	-113.58
Sample 4	-23.018	-91.21	-157.62
Sample 5	-21.136	-8.1212	-51.967
Mean	-13.801	-46.302	-95.724
Standard Error	5.2421	14.464	18.342

Table C.8: Measured temperature gradients of 1mm samples below the ice lens with outliers removed.

	-10 C/m	-50 C/m	-100 C/m
Sample 1	-8.7571	-29.293	-59.989
Sample 2	-7.9774	-86.067	-133.82
Sample 3	-8.8664	NaN	NaN
Sample 4	-30.718	-102.51	-116.22
Sample 5	NaN	-28.321	-152.92
Mean	-14.08	-61.548	-115.74
Standard Error	5.5496	19.199	20.036

Table C.9: Measured temperature gradients of 2mm samples above the ice lens with outliers removed.

	-10 C/m	-50 C/m	-100 C/m
Sample 1	NaN	NaN	NaN
Sample 2	-1.6295	-44.591	-107.58
Sample 3	-24.832	-20.491	-87.311
Sample 4	-20.994	-68.325	-124.57
Sample 5	-17.736	NaN	NaN
Mean	-16.298	-44.469	-106.49
Standard Error	5.0999	13.809	10.771

Table C.10: Measured temperature gradients of 2mm samples below the ice lens with outliers removed.

	-10 C/m	-50 C/m	-100 C/m
Sample 1	-6.3329	-145.07	-326.66
Sample 2	-42.629	-161.44	-263.38
Sample 3	-21.482	-126.09	-265.41
Sample 4	-29.044	-155.98	-450.27
Sample 5	-67.686	-178.83	-345.12
Mean	-33.435	-153.48	-330.17
Standard Error	10.379	8.7549	34.143

Table C.11: Measured temperature gradients of 3mm samples above the ice lens with outliers removed.

	-10 C/m	-50 C/m	-100 C/m
Sample 1	-3.9432	-77.547	-124.73
Sample 2	NaN	NaN	NaN
Sample 3	NaN	-29.907	-68.667
Sample 4	-32.668	-40.069	NaN
Sample 5	-35.488	-42.675	-99.668
Mean	-24.033	-47.55	-97.689
Standard Error	10.078	10.372	16.215

Table C.12: Measured temperature gradients of 3mm samples below the ice lens with outliers removed.

	-10 C/m	-50 C/m	-100 C/m
Sample 1	-34.143	-100.6	-280.08
Sample 2	-28.112	-164.79	-363.14
Sample 3	NaN	NaN	NaN
Sample 4	-10.568	-62.619	-144.19
Sample 5	NaN	NaN	NaN
Mean	-24.274	-109.33	-262.47
Standard Error	7.0707	29.815	63.818

APPENDIX D

TEMPERATURE GRADIENT ANALYSIS CODE

```
%Thermal analysis
clear all
clc
close all
%% Get Data & Calculate Linear T Gradients
date={'20211206','20211209','20220113','20220117','20220119'...%1mm
    ,'20211202','20211205','20220105','20220106','20220124'...%2mm
    ,'20211118','20211210','20211123','20220125','20220126' };%,3mm

GS=['1','2','3']; %GRain Size
TGI={'10','50','100'};
N=[0 5 5 5]; %number of samples
count=zeros(5,3,3);
rho_snow=[450 400 350];%1mm 2mm 3mm
kc_snow=((2.5.*10.^(-6)).*rho_snow.^2)-((1.23*10.^(-4)).*rho_snow)+.024; %Thermal
Conductivity

for f=1:3 % Loop through data and calculate values for each sample
    for h=(sum(N(1:f))+1):sum(N(1:f+1))
        for gi=1:3
            GSi=char(GS(f));
            datei=char(date(h));
            TGIi=char(TGI(gi));
            %count(h-sum(N(1:f)),f,gi)=1
            load([datei,'_Tgrad_',GSi,'mm_',TGIi,'C.mat']);

            %% Define Constants

            g = 9.81; % m/s^2
            R=8.31; % J/K*mol
            R_v = 461.495; % J/(K kg) Specific Gas Constant for Water Vapor
            R_d = 287.058; % J/(K kg) Specific Gas Constant for Dry Air
            L = 2.83e6; %J/kg Librecht website and from B.J. Mason, THe Physics of
Clouds, 1971 Clarendon Press
            D=2.11e-5; %m^2/s
            M=0.0180152; %kg/mol mass of water molecule
            Na = 6.022e23; %#/mol
            MH2O = M/Na; %kg per water molecule
            kb = 1.38065e-23; %(Boltzmann J/K)
            rho = 286; %kg/m^3 for round snow from Riche & Schneebeli, (get exact
density for our snow measurements)
            cp_snow = 2093.4; %J/(kg C) from Snow & Glacier Hydrology, P. Singh
            cp_ice = 1962; %J/(K kg) from Petrenko
            kc_ice = 2.4; %W/(m K) %From Physics of Ice (Petrenko) at -20C
            k_h2o = 0.016; %Thermal Conductivity of Air At H2O Saturation
            k_air = 0.024; %W/(m K) %From Wallace & Hobbs at 0C
            p = 990; %hPa local pressure near Hanover
            Diff_AB = 2.11e-5; %m^2/s Diffusivity of Water Vapor in Air
```

```
[m,x] = lin_Tgrad(mean_T(1),mean_T(12),z(1),z(end)); %Linear TG
grad_T100 = (z-x)./m;
tglin=(1/m)*1000;


Z1 = (z(3)-z(1))*(1/1000); %m height b/n tcouples
Z2 = (z(6)-z(3))*(1/1000);
Z3 = (z(10)-z(7))*(1/1000);
Z4 = (z(12)-z(10))*(1/1000);

T1_delta = -tglin*Z1; %K
T2_delta = -TGbot*Z2;
T3_delta = -TGtop*Z3;
T4_delta = -tglin*Z4;

for i=1:3

    %% Vapor Preassure
    for k=1:12
        e(k)=evappres(mean_T(k)+273.15); %Pa Murphy & Koop
        C_100_e(k)=e(k)/(R*(mean_T(k)+273.15)); %Ideal Gas Law (Also see
Pinzer et al 2012)
    end

    %% Gradient of Vapor Pressure from Riche & Schneebeli 2013
    meanT1 = (mean(mean_T(1:3))+273.15);%mean T over region
    meanT2 = (mean(mean_T(3:6))+273.15);
    meanT3 = (mean(mean_T(7:10))+273.15);
    meanT4 = (mean(mean_T(10:12))+273.15);

    e(6)=evappres(meanT2+T2_delta); %correct for Best fit TG
    e(3)=evappres(meanT2-T2_delta);
    e(10)=evappres(meanT3+T3_delta);
    e(7)=evappres(meanT3-T3_delta);

    Cz1_100 = abs(e(3)-e(1))/(Z1*kb*meanT1); %Pa/m
    Cz2_100 = abs(e(6)-e(3))/(Z2*kb*meanT2);
    Cz3_100 = abs(e(10)-e(7))/(Z3*kb*meanT3);
    Cz4_100 = abs(e(12)-e(10))/(Z4*kb*meanT4);

    %% Calculates Diffusivity of Water Vapor in Air, From W.J. Massman
1998
    D1=diffu(mean(mean_T(1:3)+273.15),p); % m^2/s
    D2=diffu(mean(mean_T(3:6)+273.15),p);
    D3=diffu(mean(mean_T(7:10)+273.15),p);
    D4=diffu(mean(mean_T(10:12)+273.15),p);

    %% Water Vapor Flux from Riche & Schneebeli 2013
    J1_100 = D1*Cz1_100*MH2O; %kg/(m^2 s)
```

```
J2_100 = D2*Cz2_100*MH2O;
J3_100 = D3*Cz3_100*MH2O;
J4_100 = D4*Cz4_100*MH2O;

%% Latent Heat Flux from Riche & Schneebeli 2013
% Calculated from measured temps
qL1 = J1_100*L; % W/m^2
qL2 = J2_100*L;
qL3 = J3_100*L;
qL4 = J4_100*L;

%% Heat Flux Bergman 2011

R1c=Z1/kc_snow(f);% Thermal resistance from conduction
R4c=Z4/kc_snow(f);
R2c=Z2/kc_snow(f);
R3c=Z3/kc_snow(f);

qc1=T1_delta/R1c;% Heat flux from conduction
qc2=T2_delta/R2c;
qc3=T3_delta/R3c;
qc4=T4_delta/R4c;

Q1=qc1+qL1;% Total heat flux in each region
Q2=Q1;
Q4=qc4+qL4;
Q3=Q4;

ql2_contr=(qL2/Q2);% % contribution to total heat flux
ql3_contr=(qL3/Q3);

Rtc2=((T2_delta.*(1-ql2_contr))/(Q2-qL2))-R2c; %Thermal Contact
Resistance
Rtc3=((T3_delta.*(1-ql3_contr))/(Q3-qL3))-R3c;

if Rtc2>0
    Rtc2_contr=1-ql2_contr-Rc2_contr; %for positive Rtc values
else
    Rtc2_contr=0; %If Rtc is negative
end

if Rtc3>0
    Rtc3_contr=1-ql3_contr-Rc3_contr;

else
    Rtc3_contr=0;
end

%% Store data
```

```
J1_total(h-sum(N(1:f)),f,gi)=J1_100;
J4_total(h-sum(N(1:f)),f,gi)=J4_100;
if TGbot<0
    Rtc2_total(h-sum(N(1:f)),f,gi)=Rtc2;
    Rtc2_contr_total(h-sum(N(1:f)),f,gi)=Rtc2_contr;
    ql2_total(h-sum(N(1:f)),f,gi)=qL2;
    Rc2_contr_total(h-sum(N(1:f)),f,gi)=Rc2_contr;
    qc2_total(h-sum(N(1:f)),f,gi)=qc2;
    TGbot_total(h-sum(N(1:f)),f,gi)=TGbot;
    ql2_contr_total(h-sum(N(1:f)),f,gi)=ql2_contr;
    qc_ice_total(h-sum(N(1:f)),f,gi)=qc_ice;
    Q1_total(h-sum(N(1:f)),f,gi)=Q1;
    J2_total(h-sum(N(1:f)),f,gi)=J2_100;
    nbot(h-sum(N(1:f)),f,gi)=1;
else
    Rtc2_total(h-sum(N(1:f)),f,gi)=nan;
    Rtc2_contr_total(h-sum(N(1:f)),f,gi)=nan;
    ql2_total(h-sum(N(1:f)),f,gi)=nan;
    Rc2_contr_total(h-sum(N(1:f)),f,gi)=nan;
    qc2_total(h-sum(N(1:f)),f,gi)=nan;
    TGbot_total(h-sum(N(1:f)),f,gi)=nan;
    ql2_contr_total(h-sum(N(1:f)),f,gi)=nan;
    qc_ice_total(h-sum(N(1:f)),f,gi)=nan;
    Q1_total(h-sum(N(1:f)),f,gi)=nan;
    J2_total(h-sum(N(1:f)),f,gi)=nan;
    nbot(h-sum(N(1:f)),f,gi)=0;
end

if TGtop<0
    Rtc3_total(h-sum(N(1:f)),f,gi)=Rtc3;
    Rtc3_contr_total(h-sum(N(1:f)),f,gi)=Rtc3_contr;
    TGtop_total(h-sum(N(1:f)),f,gi)=TGtop;
    qc_ice_total(h-sum(N(1:f)),f,gi)=qc_ice;
    ql3_contr_total(h-sum(N(1:f)),f,gi)=ql3_contr;
    Rc3_contr_total(h-sum(N(1:f)),f,gi)=Rc3_contr;
    Q1_total(h-sum(N(1:f)),f,gi)=Q1;
    J3_total(h-sum(N(1:f)),f,gi)=J3_100;
    ntop(h-sum(N(1:f)),f,gi)=1;
else
    Rtc3_total(h-sum(N(1:f)),f,gi)=nan;
    Rtc3_contr_total(h-sum(N(1:f)),f,gi)=nan;
    TGtop_total(h-sum(N(1:f)),f,gi)=nan;
    qc_ice_total(h-sum(N(1:f)),f,gi)=nan;
    ql3_contr_total(h-sum(N(1:f)),f,gi)=nan;
    Rc3_contr_total(h-sum(N(1:f)),f,gi)=Rc3_contr;
    Q1_total(h-sum(N(1:f)),f,gi)=nan;
    J3_total(h-sum(N(1:f)),f,gi)=nan;
    ntop(h-sum(N(1:f)),f,gi)=0;
end
```

```
            end
        end
    end
end

%% Solve for the Standard Error and Mean

J1_total_mean=nanmean(J1_total);
J2_total_mean=nanmean(J2_total);
J3_total_mean=nanmean(J3_total);
J4_total_mean=nanmean(J4_total);

J2_total_SE=(nanstd(J2_total)./sqrt(sum(nbot)));
J3_total_SE=(nanstd(J3_total)./sqrt(sum(nbot)));


Rtc2_contr_total_mean=nanmean(Rtc2_contr_total).*100;
ql2_contr_total_mean=nanmean(ql2_contr_total).*100;
Rc2_contr_total_mean=nanmean(Rc2_contr_total).*100;

Rtc2_contr_total_SE=(nanstd(Rtc2_contr_total)./sqrt(sum(nbot))).*100;
ql2_contr_total_SE=(nanstd(ql2_contr_total)./sqrt(sum(nbot))).*100;
Rc2_contr_total_SE=(nanstd(Rc2_contr_total)./sqrt(sum(nbot))).*100;

Rtc3_contr_total_mean=nanmean(Rtc3_contr_total).*100;
ql3_contr_total_mean=nanmean(ql3_contr_total).*100;
Rc3_contr_total_mean=nanmean(Rc3_contr_total).*100;

Rtc3_contr_total_SE=(nanstd(Rtc3_contr_total)./sqrt(sum(ntop))).*100;
ql3_contr_total_SE=(nanstd(ql3_contr_total)./sqrt(sum(ntop))).*100;
Rc3_contr_total_SE=(nanstd(Rc3_contr_total)./sqrt(sum(ntop))).*100;
```